Geoscience Frontiers 4 (2013) 517–533

Contents lists available at SciVerse ScienceDirect

China University of Geosciences (Beijing)

Geoscience Frontiers

journal homepage: www.elsevier.com/locate/gsf

Research paper

Petrology and geochemistry at the Lower zone-Middle zone transition of the Panzhihua intrusion, SW China: Implications for differentiation and oxide ore genesis

Kwan-Nang Pang [a,*], Mei-Fu Zhou [b], Liang Qi [c], Sun-Lin Chung [a], Chiu-Hong Chu [a], Hao-Yang Lee [a]

[a] Department of Geosciences, National Taiwan University, P.O. Box 13-318, Taipei 106, Taiwan
[b] Department of Earth Sciences, The University of Hong Kong, Hong Kong, China
[c] Institute of Geochemistry, Chinese Academy of Sciences, 73 Guanshui Road, Guiyang 550002, China

ARTICLE INFO

Article history:
Received 1 September 2012
Received in revised form
9 December 2012
Accepted 20 January 2013
Available online 8 February 2013

Keywords:
Fe-Ti oxides
Layered intrusion
Microgabbro
Panzhihua
Emeishan

ABSTRACT

A sequence of gabbros showing isotropic, layered and fine-grained textures is exposed in the Nalaqing mine at the southern tip of the ~260 Ma Panzhihua intrusion, SW China. The field relations, structure, texture and mineralogy of the rocks indicate that the sequence represents the transition between the Lower zone and Middle zone of the intrusion. Isotropic gabbros characteristic of the Lower zone pass upward to layered gabbros of the Middle zone through a ~5 m-thick microgabbro sheet, within and close to which small-scaled, concordant Fe-Ti oxide ore horizons are identified. Strong fractionation between HFSE and REE in a subset of samples is ascribed to cumulus titanomagnetite into which HFSE are preferentially incorporated over REE, as reflected in the parallel relations between Nb/La, Hf/Sm and Ti/Ti*. Both the isotropic and layered gabbros display cumulate textures and have similar mineral compositions ($Mg^{\#}$ of clinopyroxene = ~76–79 and $An_{59–61}$), isotopic compositions [$(^{87}Sr/^{86}Sr)_i = 0.7044–0.7045$ and $\varepsilon_{Nd}(t) = +2.4$ to $+3.9$] and trapped liquid contents inferred from Zr abundance (~17–34 ppm). However, there are substantial variations in elemental abundances (V, Cr and PGE) and ratios (Ti/V, La/Yb, Ba/Y and Cu/Pd) between the two types of gabbros, features that cannot be explained by cumulate formation from a common magma in a closed system. The microgabbros generally resemble high-Ti Emeishan basalts in major element compositions, but their low trace element abundances indicate some lost of residual liquid is inevitable despite rapid nucleation and cooling. Combined with available data and observations, we propose a model involving in-situ crystallization, followed by magma recharge and closed-system fractionation to explain the formation of texturally distinctive gabbros at Nalaqing and the evolution of the lower part of the Panzhihua intrusion.

1. Introduction

The ~260 Ma Panzhihua intrusion in the Emeishan large igneous province (ELIP) (Fig. 1) has received increasing attention in recent years partly due to the enigmatic Fe-Ti oxide ores hosted therein and in coeval intrusions in the region (Zhou et al., 2005, 2008; Pang et al., 2008a,b, 2009, 2010; Zhang et al., 2009; Hou et al., 2011, 2012b; this volume). Considerable controversy surrounds the key factor(s) responsible for ore genesis, including the probable roles of (i) a mantle source rich in Fe and Ti (Pang et al., 2008a; Zhang et al., 2009), (ii) an abnormal parental magma rich in Fe and Ti but poor in SiO_2 (Pang et al., 2008a), (iii) volatiles; either as CO_2-rich fluid from the wallrocks (Ganino et al., 2008) or small amount of dissolved H_2O and F in magma (Pang et al., 2008b, 2009), and (iv) liquid immiscibility; either between two silicate melts or involving an Fe-Ti oxide melt (Zhou et al., 2005). Besides, Ganino et al. (2008) proposed that magma–carbonate interaction in the Panzhihua intrusion might have contributed to the end-

* Corresponding author. Tel.: +886 2 33662924; fax: +886 2 23636095.
E-mail addresses: knpang@ntu.edu.tw, knpang@graduate.hku.hk (K.-N. Pang).

Peer-review under responsibility of China University of Geosciences (Beijing)

Production and hosting by Elsevier

1674-9871/$ – see front matter © 2013, China University of Geosciences (Beijing) and Peking University. Production and hosting by Elsevier B.V. All rights reserved.
http://dx.doi.org/10.1016/j.gsf.2013.01.006

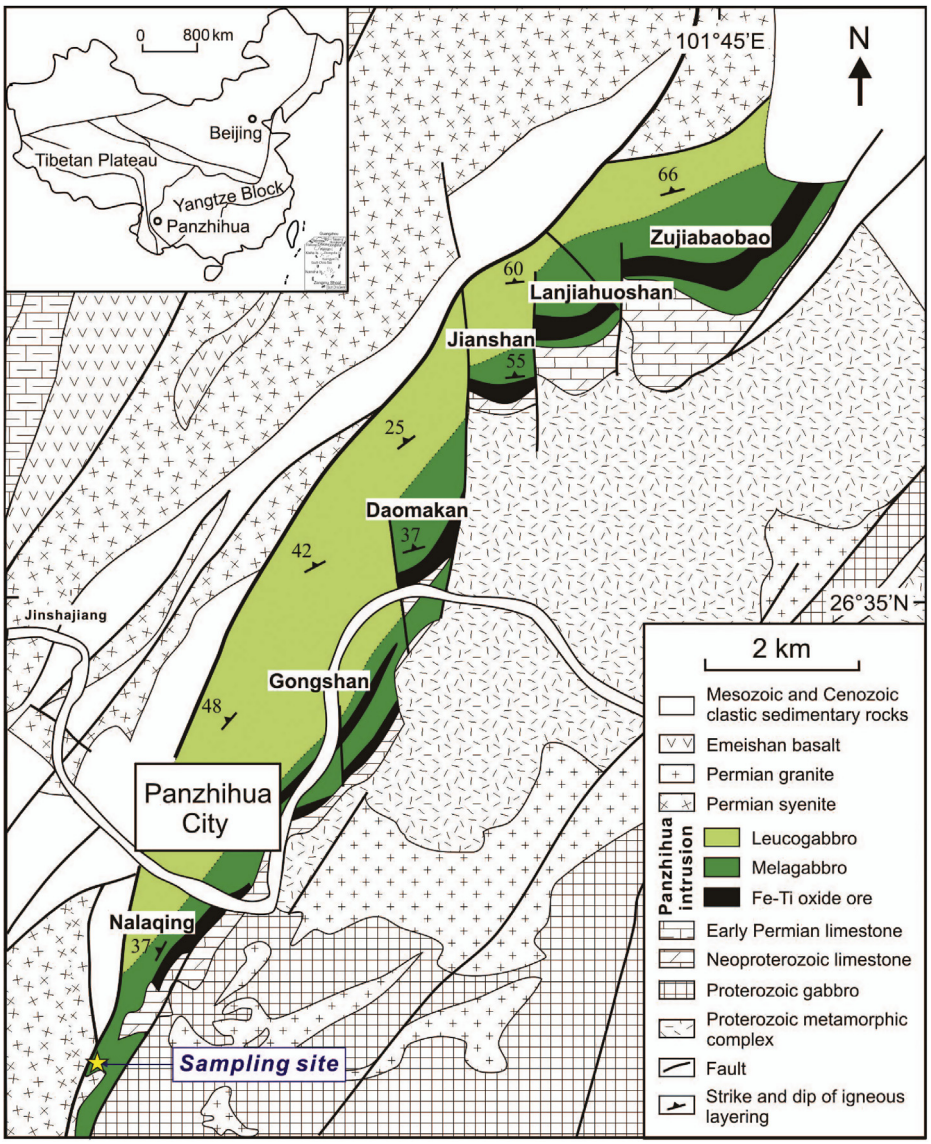

Figure 1. Geological map of the Panzhihua intrusion (modified after Zhou et al., 2005). The star denotes the sampling site in the Nalaqing mine.

Guadalupian crisis through degassing of CO_2 into the atmosphere. Thus, the Panzhihua intrusion is and will continue to be an important research target for the genesis of magmatic Fe-Ti oxide deposits and magma chamber processes associated with the intrusive facies of the ELIP.

One fundamental but unresolved issue concerning the Panzhihua intrusion and related intrusions in the region is the nature of the magmatic system (see Zhou et al., 2005; Bai et al., 2012; Shellnutt and Pang, 2012). Whether the intrusions behave as open or closed systems have profound implications for magma differentiation and oxide ore genesis. In detail, magma chambers having open system character can be further divided into those involving multiple magma pulses with limited magma extraction and those behaving as magma flow-through system (i.e. conduits). Pang et al. (2009) proposed, on the basis of plagioclase composition and bulk-rock Zr data, that the Panzhihua intrusion might have been developed from multiple magma pulses. In this study, we focus on a sequence of gabbros showing different textures corresponding to the transition between the Lower zone and Middle zone of the intrusion, a level at which the chamber might have been started to open to magma addition in view of the Pang et al.'s data (see Fig. 2). We present mineral chemical, bulk-rock major, trace, platinum-group elements (PGE) and Sr-Nd isotopic data to discuss the origin of texturally distinctive gabbros in the studied section with broader implications for the evolution of the lower part of the Panzhihua intrusion.

2. Geological background

The ~260 Ma Panzhihua intrusion (Zhou et al., 2005) is part of the end-Guadalupian Emeishan Large Igneous Province (ELIP) in the western margin of the Yangtze Block, SW China (Fig. 1, inset). The Emeishan magmatism was dominated by eruption of flood basalts presumably within 1–2 Myr, forming volcanic successions as thick as ~5 km in places (e.g. Binchuan) (Xu et al., 2001; Xiao et al., 2004). Remnants of the volcanic pile are widely present in the western Yangtze Block, the Songpan–Ganzi terrane (Song et al., 2004; Zi et al., 2010) and, the Qiangtang terrane, Tibet (Chung et al., 1998), and Song Da region of Vietnam (Wang et al., 2007; Anh et al., 2011). Minor picrites and silicic volcanic rocks were found in the volcanic

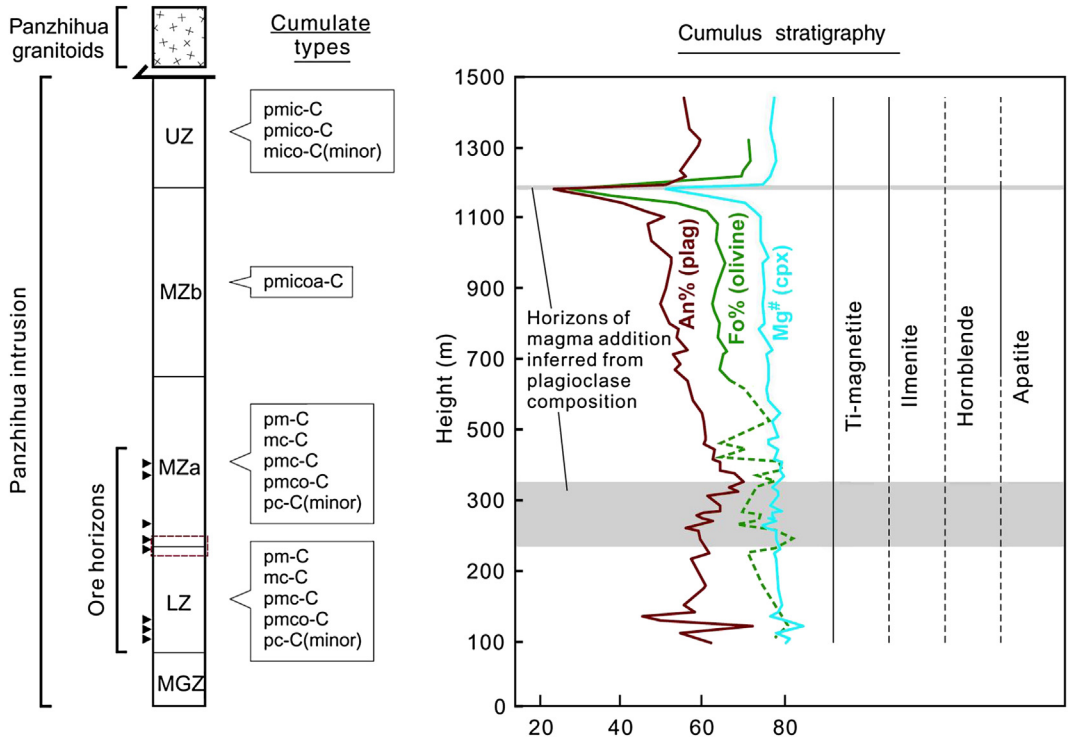

Figure 2. A simplified stratigraphic column of the Panzhihua intrusion, showing the zonal division and the variations in cumulate types, cumulus minerals and their compositions. The cumulate nomenclature of Irvine (1982) was used by which rocks are named according to the first letter of the main minerals followed by "-C" meaning cumulus: plagioclase (p), magnetite (m), ilmenite (i), clinopyroxene (c), olivine (o) and apatite (a). The red dotted rectangle denotes the stratigraphic level of the studied section at Nalaqing. Data for cumulus mineral compositions are after Pang et al. (2009). (For interpretation of the references to color in this figure legend, the reader is referred to the web version of this article.)

successions (Chung and Jahn, 1995; Zhang et al., 2006; Li et al., 2012). The intrusive facies of the ELIP mainly crops out in the central–western part of the province, including mafic–ultramafic intrusions and granitic plutons. Some of the mafic–ultramafic intrusions host Ni-Cu-(PGE) sulfide or Fe-Ti-(V) oxide mineralization. The granitic plutons include granites and syenites, and many of them are contemporaneous with the mafic intrusions in a given location. In addition, crustally derived granitic rocks are present in the region (Zhong et al., 2007; Shellnutt et al., 2011). Generally, the Emeishan magmatism is widely attributed to impingement of a mantle plume at the base of the lithosphere from below (Chung and Jahn, 1995; Xu et al., 2001, 2004; Xiao et al., 2004; Zhang et al., 2006).

The Panzhihua intrusion is one of the several layered intrusions that host Fe-Ti oxide ores in the central–western ELIP (see Pang et al., 2010 for review). Its geology was described in detail by Ma et al. (2001) and summarized by Zhou et al. (2005). The ~19 km-long elongate intrusion is tilted to the northwest and composed of ~2 km-thick gabbroic cumulates. It was emplaced in Neoproterozoic dolomitic limestones, which were transformed into marble as a result of contact metamorphism, and was unconformably overlain by Triassic clastic sedimentary rocks. The thickness of the contact aureole is estimated to be ~300 m (Ganino et al., 2008). From the base upwards, the intrusion was divided into a Marginal zone (MGZ), Lower zone (LZ), Middle zone (sub-zones MZa and MZb) and Upper zone (UZ) (Pang et al., 2008a, 2009) (Fig. 2). The MGZ is dominated by microgabbros and the LZ by coarse-grained and isotropic gabbros with local pegmatitic facies. These zones contain extensive Fe-Ti oxide ores occurring as massive to semi-massive bodies with thickness up to a few tens of meters. Rocks from the MZa and the overlying zones display well-developed modal layering marked by the relative abundance between plagioclase and clinopyroxene and/or Fe-Ti oxides. Oxide-rich layers are also present in the MZa but are much less extensive compared to their counterparts in the MGZ and LZ. The base of the MZb is marked by the appearance of cumulus apatite, whereas the overlying UZ does not contain cumulus apatite. One notable feature of the Panzhihua intrusion is its association with large volumes of coeval granitic rocks (Shellnutt and Zhou, 2007; Zhong et al., 2009; Shellnutt and Jahn, 2010). However, the contacts of the UZ against these granitic rocks and against the Triassic strata are not exposed.

The Nalaqing mine is located in the southern tip of the Panzhihua intrusion (26°32.9′N, 101°40.7′E) (Fig. 1). A section striking SE–NW with length of ~35 m is exposed as a result of earlier mining prospects. Generally, coarse-grained, isotropic gabbros crop out in the southeastern part of the section and pass into medium-grained layered gabbros in the northwestern part through a microgabbro sheet with thickness of ~5 m (Fig. 3). The isotropic gabbros are largely structureless but locally contain randomly distributed pegmatitic masses that are mineralogically similar to and in transitional contact with their host rocks (Fig. 4a–c). The layered gabbros consist of centimeter-scaled modal layering, which is defined chiefly by the relative abundances of plagioclase and clinopyroxene + Fe-Ti oxides (Fig. 4d–f). In addition, plagioclase shows igneous lamination at the direction of the layering. A wehrlite dyke was found cutting the layered gabbro (Fig. 3), although its orientation does not differ significantly from the direction of igneous layering. It is fine-grained, grayish and structureless. This dyke might be related to the wehrlitic dykes identified close to the intrusive contact (see Hou

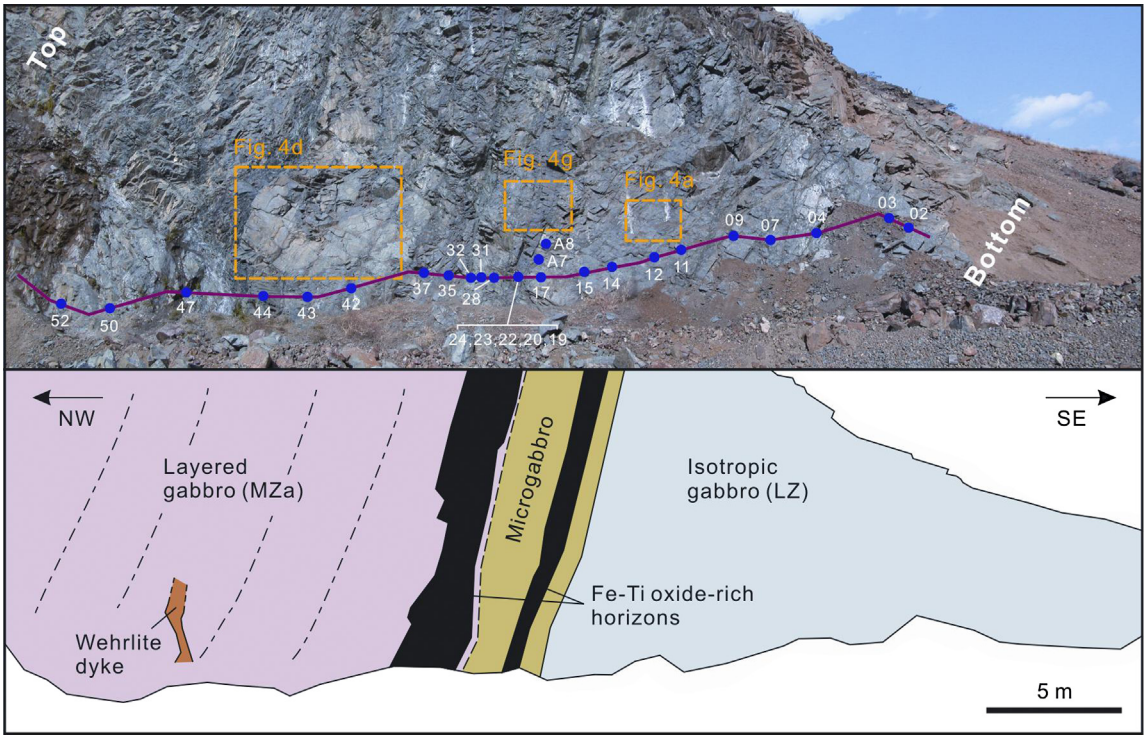

Figure 3. The studied section in the Nalaqing mine of the Panzhihua intrusion, showing the sample spots (blue dots with numbers in the upper frame). The lower frame is a schematic sketch, showing that the isotropic gabbros are separated from the layered gabbros by a ~5 m-thick horizon of microgabbros, near which two main Fe-Ti oxide ore horizons are found. Note the concordance between the microgabbros, layered gabbros and oxide ore horizons. Enlarged views of the dotted rectangles in the upper frame are shown in Fig. 4.

et al., 2012b). However, the dyke constitutes only a minor portion relative to the volume of the entire section. In other words, the majority of the layered rocks are gabbroic. The layering is at high angles dipping NW, an orientation similar to that measured elsewhere in the intrusion, indicating post-solidification tilting. The microgabbro sheet in between the isotropic and layered gabbros is intact, homogeneous and structureless (Fig. 4g–i). It is in sharp contact against the underlying isotropic rocks and the contact against the overlying layered gabbros is either sharp or gradational. Within the microgabbro sheet, a ~50 cm-thick Fe-Ti oxide ore horizon and many similar but thinner oxide-rich stringers are observed and they are in sharp contact against the microgabbros (Fig. 4g). The oxide ores are dense and contain medium- to coarse-grained, embedded silicate grains whose mineralogy is similar as in the gabbros. These silicate minerals are volumetrically minor compared to the ore minerals, but their distributions are irregular in places and in some case showing a preferred orientation as the layered gabbros. Another oxide ore horizon, with thickness ~80 cm, is identified just above (referred to as the original configuration and will be used throughout the manuscript unless otherwise noted) the contact between the microgabbros and layered gabbros, and display similar features as the one occurring in the microgabbros. Based on the stratigraphic division noted above, our field and petrographic observations (see later descriptions), the studied section at Nalaqing represents the transition between the upper LZ and the lower MZa of the Panzhihua intrusion.

3. Petrography

The isotropic gabbros contain cumulus clinopyroxene (~40–45%), plagioclase (~40–45%) and Fe-Ti oxides (~5–10%) that are randomly oriented, with minor hornblende and sulfides (Fig. 4b and c). Clinopyroxene and plagioclase occur as large crystals in straight or slightly ragged boundaries to each other. Although large crystals dominate, many of them coexist with fine-grained aggregates of the same mineral, which exhibit ~120° triple junctions. This texture, together with the complex polysynthetic twinning observed from some large plagioclase grains, indicates that the rocks underwent recrystallization. The Fe-Ti oxides occur as amoeboid aggregates of magnetite and ilmenite, with sizes much smaller than the clinopyroxene and plagioclase grains, at the silicate grain boundaries. Many clinopyroxene grains contain Fe-Ti oxide lamellae oriented along their prismatic cleavages (Fig. 4c). Oxy-exsolved ilmenite lamellae within magnetite are common. Secondary hornblende is present in trace amounts as fine, irregular masses either at grain boundaries or completely enclosed by clinopyroxene (Fig. 4c). Olivine is completely absent in these rocks. Overall, the textures and mineralogy of the isotropic gabbros are similar to those in the LZ of the Panzhihua intrusion (see Pang et al., 2008a, 2009).

The cumulus assemblage of the layered gabbros is similar to that of the isotropic gabbros, except the sporadic occurrence of minor olivine and the generally higher Fe-Ti oxide abundance (Fig. 4e and f). One notable feature is that plagioclase in the layered gabbros commonly displays a planar lamination, whereas that in the isotropic gabbros does not. Coexistence of clinopyroxene or plagioclase grains with large size difference is also noted as in the isotropic gabbros. Reaction rims of hornblende and, to a lesser extent, olivine are observed around many of these embedded silicate crystals. The wehrlite contains cumulus olivine, clinopyroxene and minor Fe-Ti oxides but largely plagioclase-free. With respect to texture and mineralogy, the layered gabbros

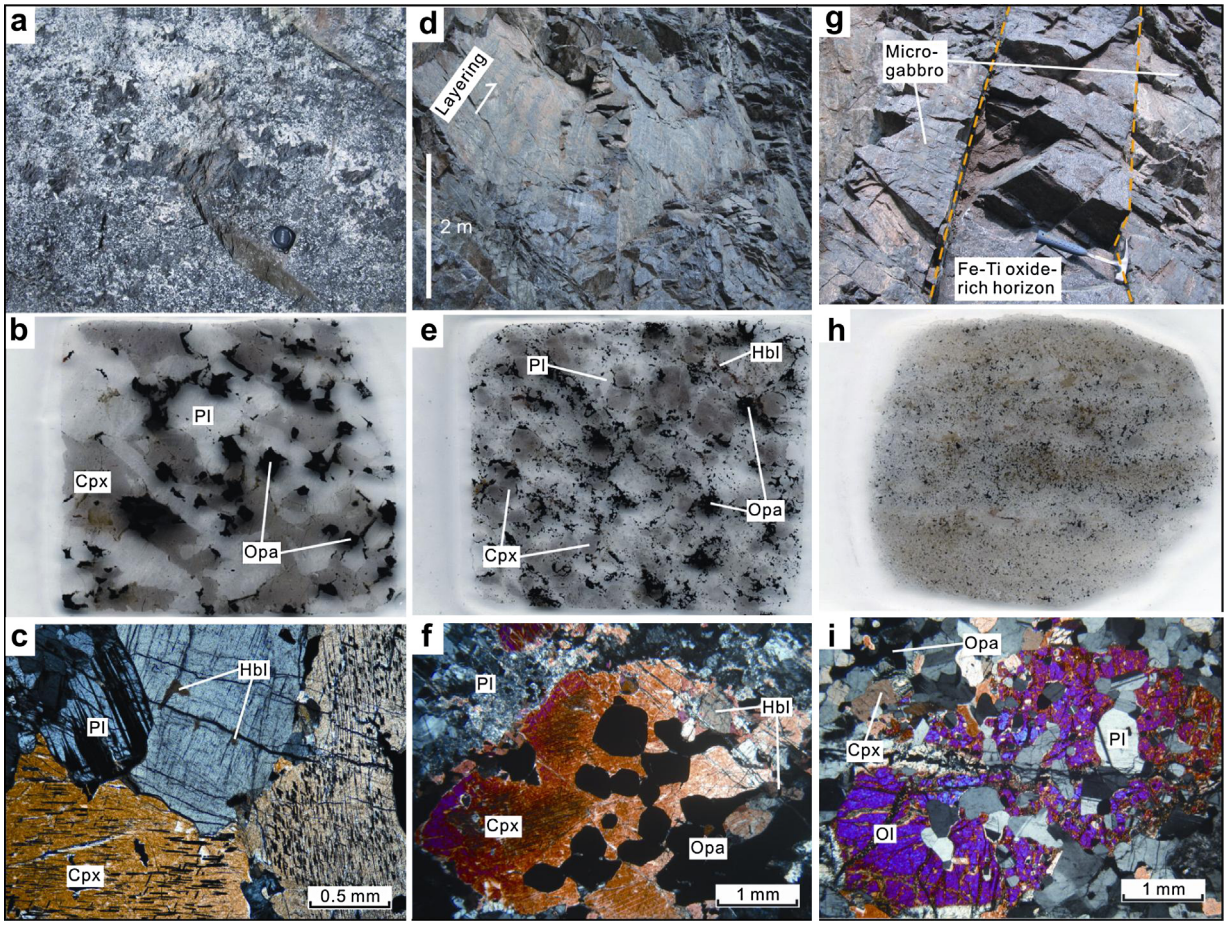

Figure 4. Field occurrences, thin section scans and photomicrographs of rocks from the studied section. a: A pod of pegmatitic gabbro in isotropic gabbro. b: A thin section scan of an isotropic gabbro. c: Coarse clinopyroxene and plagioclase grains that are in smooth or ragged boundaries to each other in an isotropic gabbro (sample LQ06). d: Modal layering marked by alternative layers rich in plagioclase and in mafic silicates + Fe-Ti oxides. e: A thin section scan of a layered gabbro. f: Cumulus Fe-Ti oxides in a large clinopyroxene crystal coexisting with variably-altered plagioclase in a layered gabbro (sample LQ34). g: An oxide-rich horizon (center) and numerous oxide-rich stringers (left) intercalated by microgabbros. h: A thin section scan of a microgabbro. i: Poikilitic olivine enclosing (aggregated) plagioclase grains in a microgabbro (sample LQA5). The width of each thin section scan is ~2.5 cm.

resemble those in the MZa of the intrusion (see Pang et al., 2008a, 2009).

The microgabbros are characterized by fine-grained and equigranular textures (Fig. 4h). They contain clinopyroxene, plagioclase, titanomagnetite, ilmenite and trace amount of hornblende with or without olivine. When present, olivine occurs as poikilitic masses enclosing irregular plagioclase grains (Fig. 4i). The microgabbros are characterized by an equigranular texture with grain sizes between 0.2 and 0.5 mm. In places, they contain large grains of clinopyroxene and plagioclase set in a fine-grained matrix of the above minerals. Oxide minerals in the microgabbros are largely free of micro-intergrowths.

The Fe-Ti oxide ores consist of massive aggregates (>50%) of magnetite and ilmenite with variable amounts of embedded clinopyroxene + plagioclase ± olivine grains, many of which have a preferred orientation, and minor sulfides. However, the amounts, types and distribution of the silicate grains are highly variable, even within a given thin section. The oxide ores are characterized by a granular and massive texture consisting of medium to coarse polygonal grains of titanomagnetite and ilmenite, with typical sizes ranging between 1 and 1.5 mm. Most boundaries between titanomagnetite and ilmenite are straight to slightly curved and meet at distinct triple junctions with ~120° interfacial angles. Titanomagnetite is dominant over ilmenite at estimated ratios of ~3:1–4:1 and it contains fine micro-intergrowths of ulvöspinel, ilmenite and hercynitic spinel.

4. Analytical methods

Twenty-eight out of fifty-three samples collected from the Nalaqing mine were selected for geochemical analyses. They were carefully cut with a diamond-impregnated brass blade, crushed in a steel jaw crusher and pulverized in agate mortars. Pulverized samples were analyzed for major and trace elements and a subset of them were analyzed for PGE and Sr-Nd isotopes. Mineral compositions were determined on polished thin sections for selected samples.

4.1. Electron microprobe analyses

Mineral compositions were determined by a CAMECA SX50 electron microprobe at Indiana University, Bloomington, U.S.A. Major elements were analyzed using wavelength-dispersive method at an accelerating voltage of 15 kV, beam current of 20 nA, a focused beam of 1 μm diameter and a peak counting time of 20 s. Minor elements (Cr, Ti and V in clinopyroxene, Ni in olivine,

and Fe in plagioclase) were analyzed using the same parameters except a higher current of 100 nA and longer peak counting time of 50 s. Detection limits of 100 ppm Cr, 120 ppm Ni, 100 ppm Ti, 100 ppm V, and 300 ppm Fe can be achieved under these conditions. Corrections were made for the interferences of Ti with V, and of V with Cr. The accuracy of the analyses was monitored using mineral standards and the precision was generally better than 2% for most elements.

4.2. Bulk-rock geochemical analyses

Abundances of major, trace and platinum-group elements (PGE) were mainly determined at Department of Earth Sciences, The University of Hong Kong. LOI was obtained by routine procedures. Sulfur abundance was determined by a gravimetric method at the University of Hong Kong. Major element oxides were determined on fused glass disks by wavelength-dispersive X-ray fluorescence spectrometry (WD-XRFS) on a Philips PW2400 spectrometer. For the Fe-Ti oxide ore samples, XRF analysis is unsuitable and the major and some transition elements were measured by wet chemistry, gravimetry and inductively coupled plasma-optical emission spectrometry (ICP-OES) at Institute of Geochemistry, Chinese Academy of Sciences, Guiyang, China. Concentrations of trace elements were determined by inductively coupled plasma-mass spectrometry (ICP-MS) on nebulized solutions using a VG Plasma-Quad Excell ICP-MS after 2-day closed-beaker digestion of pulverized sample using a mixture of HF and HNO_3 in high-pressure bombs (Qi et al., 2000). Pure elemental standard solutions were used for external calibration and AMH-1 (Mount Hood andesite) and OU-6 (Penrhyn slate) were used as reference materials. The accuracy of the XRF analyses is estimated to be ±2% (relative) for major oxides present in concentrations greater than 0.5 wt.% and ±5% (relative) for minor oxides present in concentrations greater than 0.1%. The accuracy of the ICP-MS analyses is estimated to be better than ±5% (relative) for most elements.

Concentrations of PGE were determined by ICP-MS using an improved Carius tube method (see Qi et al., 2007; Qi and Zhou, 2008a). Each pulverized sample was digested in 30 mL *aqua regia* in a 120 mL pre-cleaned Carius tube in which an appropriate amount of enriched isotope spike solution containing ^{193}Ir, ^{101}Ru, ^{194}Pt and ^{105}Pd was added. The tube was then sealed, placed into a custom-made high-pressure autoclave filled with water to prevent potential explosion, and heated to 280 °C for ~12 h. After cooling, the sample solution was centrifuged, extracted and treated by Te-coprecipitation to pre-concentrate PGE (Qi et al., 2004, 2007). Osmium data are not reported because of its volatility during sample preparation (Sun et al., 2001). The reference material WPR-1 (PGE-rich peridotite) was used to monitor the reliability of data. The accuracy of the PGE analyses is estimated to be better than ±15% (relative).

4.3. Sr-Nd isotopic analyses

Isotopic compositions of Sr and Nd were determined on purified solutions by a Thermo Electron Finnigan Neptune multi-collector ICP-MS at Department of Geosciences, National Taiwan University, Taiwan (see Lee et al., 2012 for detailed analytical procedures).

Table 1
Representative electron microprobe analyses of minerals from the studied section at Nalaqing.

Sample	Mineral[a]	Comment	SiO_2	TiO_2	Al_2O_3	Cr_2O_3	FeO	MnO	MgO	CaO	Na_2O	K_2O	NiO	V_2O_3	Total	D.I.[b]
Isotropic gabbro																
LQ04	Cpx	Granular-core	50.52	1.16	3.60	Bdl[c]	7.31	0.26	14.41	21.89	0.51	Bdl	–	0.04	99.74	77.8
LQ04	Cpx	Granular-core	49.32	1.42	3.65	Bdl	7.67	0.25	14.27	22.01	0.48	0.01	–	0.05	99.16	76.8
LQ07	Cpx	Granular-core	49.27	1.64	3.55	Bdl	8.55	0.19	14.42	21.06	0.52	0.01	–	0.04	99.29	75.1
LQ07	Cpx	Granular-core	49.31	1.39	3.81	0.02	7.57	0.19	14.37	21.39	0.48	Bdl	–	0.05	98.61	77.2
LQ04	Plag	Granular-core	53.30	–	30.04	–	0.16	–	–	11.83	4.60	0.19	–	–	100.12	58.7
LQ04	Plag	Granular-core	52.02	–	30.35	–	0.17	–	–	12.63	4.34	0.16	–	–	99.66	61.7
LQ07	Plag	Granular-core	53.36	–	29.75	–	0.22	–	–	11.89	4.62	0.23	–	–	100.07	58.7
LQ07	Plag	Granular-core	52.85	–	30.06	–	0.12	–	–	12.42	4.48	0.25	–	–	100.18	60.5
Microgabbro																
LQ17	Olivine	Poikilitic	36.14	–	–	–	30.41	0.53	32.55	0.02	–	–	0.10	–	99.76	65.6
LQ17	Olivine	Poikilitic	35.77	–	–	–	30.58	0.50	33.24	0.07	–	–	0.12	–	100.27	65.9
LQA5	Olivine	Poikilitic	34.44	–	–	–	30.19	0.56	33.20	0.04	–	–	0.08	–	98.50	66.2
LQA5	Olivine	Poikilitic	35.46	–	–	–	30.07	0.41	32.80	0.06	–	–	0.10	–	98.89	66.1
LQA5	Cpx	Fine-grained	50.72	0.83	2.94	0.01	8.24	0.26	14.87	22.02	0.47	Bdl	–	0.05	100.44	76.3
LQ17	Cpx	Fine-grained	49.91	1.39	3.21	0.02	8.49	0.19	14.94	20.27	0.42	0.01	–	0.06	98.95	75.8
LQ32	Cpx	Fine-grained	51.24	0.52	1.92	0.02	9.46	0.24	14.39	21.06	0.38	0.03	–	0.05	99.31	73.1
LQA5	Plag	Inclusion in olivine	52.92	–	30.08	–	0.41	–	–	12.17	4.62	0.20	–	–	100.39	59.3
LQ17	Plag	Inclusion in olivine	53.54	–	29.45	–	0.31	–	–	11.69	4.89	0.30	–	–	100.17	56.9
LQ32	Plag	Fine-grained	56.73	–	27.89	–	0.12	–	–	9.59	5.85	0.46	–	–	100.64	47.5
Layered gabbro																
LQ35	Olivine	Poikilitic	37.82	–	–	–	21.63	0.34	40.06	0.11	–	–	0.02	–	99.98	76.8
LQ40	Olivine	Poikilitic	36.76	–	–	–	27.11	0.46	35.90	0.07	–	–	0.01	–	100.31	70.2
LQ40	Olivine	Poikilitic	37.18	–	–	–	24.17	0.40	38.02	0.04	–	–	0.00	–	99.80	73.7
LQ35	Cpx	Granular-core	50.84	1.17	3.95	Bdl	6.04	0.17	14.35	22.97	0.60	0.01	–	0.05	100.18	80.9
LQ40	Cpx	Granular-core	49.69	1.58	4.15	Bdl	7.59	0.20	14.68	21.30	0.52	Bdl	–	0.05	99.82	77.6
LQ52	Cpx	Granular-core	49.89	1.33	3.66	0.01	8.04	0.33	14.50	21.08	0.50	Bdl	–	0.05	99.42	76.3
LQ35	Plag	Granular-core	52.52	–	30.48	–	0.06	–	–	13.13	4.18	0.11	–	–	100.47	63.4
LQ40	Plag	Granular-core	52.96	–	29.98	–	0.12	–	–	12.00	4.64	0.22	–	–	99.92	58.9
LQ52	Plag	Granular-core	52.15	–	30.49	–	0.22	–	–	12.43	4.61	0.16	–	–	100.06	59.8

[a] Cpx = clinopyroxene, Plag = plagioclase.
[b] D.I. = differentiation index (Fo of olivine, $Mg^{\#}$ of clinopyroxene and An of plagioclase).
[c] Bdl = below detection limit.

Chemical separation of Sr and Nd was performed using routine cation-exchange column techniques after repeated digestion of pulverized sample by HF–HNO_3 mixtures in closed Telfon beakers. The measured isotopic ratios $^{87}Sr/^{86}Sr$ and $^{143}Nd/^{144}Nd$ were corrected for mass fractionation with the exponential law using $^{88}Sr/^{86}Sr = 8.375209$ and $^{146}Nd/^{144}Nd = 0.7219$, respectively. Measurements of the standard SRM987 over the course of the analyses averaged 0.710256 ± 33 ($n = 4$) and those of the standard JNdi-1 averaged 0.512087 ± 11 ($n = 5$).

5. Results

5.1. Lithologic variations

Representative analyses of olivine, clinopyroxene and plagioclase in the samples are listed in Table 1. The lack of significant zoning in these minerals is evident by the largely uniform core-and-rim compositions. In each sample, the forsterite content of olivine (Fo), $Mg^{\#}$ of clinopyroxene and anorthite content of plagioclase (An) commonly vary between 2 and 5 mol%. Clinopyroxene and plagioclase in the isotropic and layered gabbros have similar compositional ranges of $Mg^{\#} = \sim 76–79$ and $An_{59–61}$ (Fig. 5a). Compared to these ranges, the mineral compositions of one microgabbro (sample LQ32) are relatively evolved (average $Mg^{\#}$ of clinopyroxene = 72 and An_{49}), whereas those of another two microgabbro samples are only slightly more evolved (Fig. 5a). These two samples contain olivine of $\sim Fo_{66}$ and with relatively high Ni contents ranging from 610 to 940 ppm. Olivine in other samples has relatively higher Fo and low Ni contents (Fig. 5b).

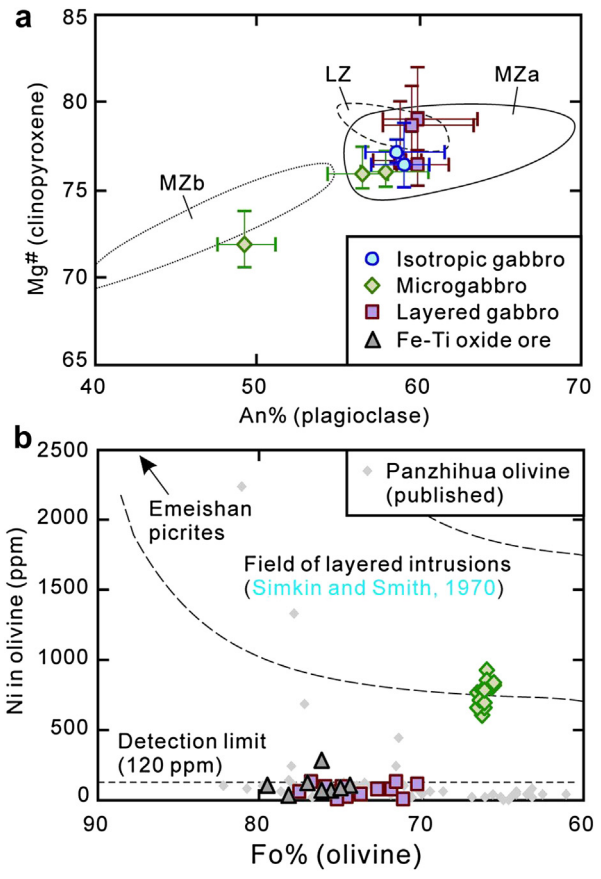

Figure 5. Mineral compositions for selected samples in the studied section at Nalaqing. a: $Mg^{\#}$ of clinopyroxene versus An of plagioclase. Data for LZ, MZa and MZb of the Panzhihua intrusion by Pang et al. (2009) are shown for reference. b: Ni content versus Fo of olivine. Gray diamonds denote published data by Pang et al. (2008b) and Pang et al. (2009) and the region bounded by dashed lines represents olivine from layered intrusions (after Simkin and Smith, 1970).

The major and trace element, and PGE data for the samples are listed in Table 2. The isotropic gabbros have relatively uniform major element compositions with inter-sample variations of several weight percents, including SiO_2 (36.6–40.4 wt.%), TiO_2 (3.7–5.3 wt.%), Al_2O_3 (9.5–14.8 wt.%), total iron as Fe_2O_3 (18.2–24.8 wt.%), MgO (4.7–7.9 wt.%), CaO (9.2–12.7 wt.%) and Na_2O (1.6–2.9 wt.%) (Fig. 6a–f). Compared to the isotropic gabbros, the layered gabbros have lower SiO_2, Al_2O_3, CaO, Na_2O, K_2O and higher TiO_2 and Fe_2O_3 (Fig. 6a–c and e–g). The microgabbros also have rather uniform major element concentrations except Na_2O and K_2O (Fig. 6f and g); they have higher SiO_2 and $Mg^{\#}$, and lower TiO_2 and Fe_2O_3, than the isotropic and layered gabbros (Fig. 6a, b and h). The Fe-Ti oxide ores have very high TiO_2 (10.5–15.6 wt.%) and total iron as Fe_2O_3 (58.7–73.0 wt.%) and low in the rest major element oxides (Fig. 6a–h). The wehrlite sample is marked by high MgO (22.7 wt.%), $Mg^{\#}$ (73.4) and low Al_2O_3 (4.2 wt.%) and Na_2O (0.3 wt.%). On the major element diagrams, most data plot between a melanogabbroic pole (clinopyroxene:plagioclase = 2:1), a leucogabbroic pole (clinopyroxene:plagioclase = 1:2) and the primary titanomagnetite composition estimated by Pang et al. (2008a) (see Fig. 6 for details), indicating that the observed variations can be accounted for by variable amounts of cumulus titanomagnetite in a gabbroic assemblage. On a V versus TiO_2 diagram, some data follow a positive trend toward the primary titanomagnetite composition, whereas some others plot on another positive trend with a gentler slope, pointing to a mixed control by titanomagnetite and ilmenite (Fig. 7a). Most data show a positive trend between Cr and TiO_2 (Fig. 7b), suggesting that the cumulus titanomagnetite contains significant Cr in the level of several hundred ppm. The microgabbro and wehrlite data show a vertical trend on the same diagram (Fig. 7b), consistent with control by chrome spinel. The S contents of the samples are high and variable (~0.1–5.6 wt.%) and are not correlated with concentrations of Ni, Cu or Pd (Fig. 7c–e), which could be related to the addition of S in a late- or post-magmatic stage. However, samples having high Cu contents tend to have moderate to high S contents. A positive trend is observed on a log-log plot of Pd versus Ir (Fig. 6f), indicating that the Pt-subgroup PGE (PPGE) and the Ir-subgroup PGE (IPGE) are likely controlled by the same phase. The wehrlite sample has high concentration of Ir relative to Pd (Fig. 6f), probably related to the presence of IPGE-rich alloy.

Generally, the absolute abundances of incompatible trace elements in the samples follow the order: microgabbros > isotropic and layered gabbros > Fe-Ti oxide ores (Table 2). The range of Zr contents of the samples is ~16–41 ppm, which corresponds to ~11–27% trapped liquid component with reference to high-Ti Emeishan basalts with >6 wt.% MgO and >150 ppm Zr (Xu et al., 2001; Xiao et al., 2004). The chondrite-normalized rare earth element (REE) patterns for the isotropic gabbros, microgabbros and layered gabbros are characterized by either flat or slightly positive slopes from light to middle REE, negative slopes from middle to heavy REE and positive Eu anomaly (Fig. 8a–c). The REE patterns for the Fe-Ti oxide ores are less coherent than the above samples, probably related to their low trace element abundances. On mantle-normalized trace element diagrams, the isotropic gabbros, microgabbros and layered gabbros show depletions in Rb, Th, and U, and enrichments in Pb and Ti relative to elements with similar incompatibilities (Fig. 9a–c). Another notable feature is the strong fractionation between REE and HFSE, which is observed in the

Table 2
Geochemical data for rocks from the studied section at Nalaqing.

	Isotropic gabbro									Microgabbro					
Sample	LQ02	LQ03	LQ04	LQ07	LQ09	LQ11	LQ12	LQ14	LQ15	LQ17	LQA7	LQA8	LQ28	LQ31	LQ32
Major oxides (wt.%)															
SiO_2	40.38	36.64	38.05	38.90	38.20	39.48	39.47	36.88	38.96	44.65	43.92	42.62	43.46	47.13	47.96
TiO_2	3.66	5.26	4.64	4.60	4.75	5.03	4.29	4.79	3.96	2.48	2.84	2.47	2.91	2.79	2.74
Al_2O_3	13.53	9.49	10.88	11.46	11.62	13.22	15.12	14.27	14.84	12.92	12.65	13.31	10.14	13.09	11.93
Fe_2O_3[b]	18.20	24.78	21.51	21.16	21.60	20.95	19.89	23.06	19.99	14.47	15.80	13.75	16.18	12.71	13.45
MnO	0.16	0.21	0.19	0.19	0.18	0.18	0.15	0.15	0.17	0.18	0.19	0.17	0.18	0.17	0.19
MgO	6.39	7.92	7.62	7.84	7.07	6.11	4.98	4.73	6.72	8.44	8.32	7.60	11.23	7.73	8.56
CaO	12.68	11.92	12.47	12.66	11.82	10.86	9.86	10.00	9.24	13.48	12.91	15.09	12.95	10.96	11.90
Na_2O	1.99	1.56	1.69	1.62	2.09	2.43	2.88	2.32	2.24	1.98	2.11	1.62	1.44	2.74	2.52
K_2O	0.17	0.10	0.13	0.15	0.15	0.14	0.20	0.21	0.21	0.09	0.10	0.03	0.11	0.19	0.25
P_2O_5	0.00	0.00	0.00	0.00	0.00	0.00	0.00	0.00	0.00	0.00	0.00	0.00	0.00	0.00	0.00
LOI	1.40	0.90	0.70	0.57	1.47	1.50	1.30	1.13	0.87	1.37	0.53	3.36	1.27	2.30	0.37
S	2.68		1.49	3.1		2.61			0.74	1.15					0.05
Trace elements (ppm)															
Li	1.64	1.72	1.75	1.62	2.52	3.23	3.42	4.15	1.99	2.04	2.98	1.57	2.48	2.50	1.80
Sc	28.0	34.3	31.8	32.7	29.9	25.8	22.5	18.0	17.3	35.1	34.1	29.8	29.6	31.0	30.7
V	139	543	76.6	54.6	117	81.7	168	653	112	306	334	97.8	320	426	449
Cr	2.20	2.31	1.05	2.11	2.85	4.71	2.44	17.8	5.50	262	237	183	410	155	236
Co	76.9	101	75.3	79.8	85.4	84.8	77.4	94.5	86.1	65.6	74.7	63.7	89.2	66.5	66.7
Ni	23.5	37.4	33.5	71.1	73.3	72.0	70.2	105	61.4	131	176	154	138	97	104
Cu	59.8	66.2	46.4	190	246	274	230	498	189	17.5	64.0	32.8	76.8	12.9	13.0
Zn	119	144	153	135	148	126	137	154	136	99.6	109	98.5	106	131	115
Ga	21.9	20.1	20.1	21.5	19.6	19.4	21.7	25.2	21.9	21.3	20.3	20.8	16.9	20.1	19.8
Rb	2.60	1.67	2.08	2.75	2.18	1.81	2.33	2.17	2.41	1.13	1.38	0.62	1.65	2.43	1.52
Sr	582	338	440	481	382	468	590	752	645	478	488	447	433	742	570
Y	6.53	7.62	7.01	7.49	7.33	6.42	5.00	4.87	4.16	10.9	11.6	10.1	9.94	13.8	13.4
Zr	17.1	21.3	19.4	19.8	23.9	27.3	19.6	26.6	20.6	17.2	18.1	16.2	22.8	40.6	38.6
Nb	1.32	1.72	1.65	1.72	2.27	3.63	2.15	3.08	2.35	0.70	0.93	0.79	1.20	6.78	4.28
Cs	0.14	0.18	0.13	0.11	0.24	0.15	0.24	0.16	0.12	0.08	0.11	0.06	0.09	0.09	0.10
Ba	93.8	69.1	74.1	79.2	121	93.5	161	140	112	61.0	57.0	21.8	57.1	133	132
La	2.05	1.70	1.68	1.84	2.34	2.50	2.27	2.46	2.17	1.87	1.85	1.64	1.89	3.82	3.58
Ce	5.16	5.32	4.93	5.22	6.20	6.30	5.41	5.73	4.91	5.62	5.68	5.02	6.20	10.4	10.0
Pr	0.92	0.94	0.96	0.99	1.10	1.05	0.87	0.92	0.80	1.20	1.16	0.98	1.26	1.88	1.87
Nd	5.28	5.56	5.40	5.61	5.79	5.54	4.43	4.86	3.89	6.84	6.83	5.70	7.15	9.98	9.88
Sm	1.62	1.78	1.71	1.73	1.77	1.59	1.22	1.26	1.03	2.19	2.35	2.02	2.37	2.98	3.12
Eu	0.91	0.92	0.90	0.89	0.96	0.87	0.88	0.78	0.84	1.14	1.14	1.00	0.87	1.33	1.34
Gd	1.79	1.98	1.95	1.92	1.86	1.73	1.32	1.39	1.05	2.73	2.76	2.44	2.47	3.15	3.01
Tb	0.25	0.33	0.30	0.33	0.31	0.27	0.19	0.20	0.17	0.43	0.44	0.40	0.39	0.54	0.53
Dy	1.36	1.69	1.41	1.60	1.62	1.37	1.04	1.01	0.87	2.45	2.54	2.22	2.13	2.93	2.77
Ho	0.26	0.30	0.28	0.31	0.29	0.26	0.19	0.20	0.16	0.47	0.50	0.44	0.41	0.54	0.55
Er	0.66	0.77	0.73	0.74	0.73	0.70	0.47	0.52	0.43	1.21	1.32	1.13	1.06	1.40	1.50
Tm	0.08	0.09	0.08	0.08	0.08	0.07	0.05	0.06	0.05	0.14	0.15	0.14	0.13	0.18	0.18
Yb	0.44	0.58	0.48	0.56	0.55	0.45	0.37	0.34	0.32	0.86	0.91	0.76	0.81	1.10	1.13
Lu	0.07	0.07	0.07	0.08	0.07	0.07	0.05	0.05	0.04	0.11	0.13	0.12	0.11	0.16	0.16
Hf	0.67	0.85	0.75	0.82	0.88	1.05	0.71	0.86	0.69	0.88	0.90	0.79	1.02	1.58	1.46
Ta	0.13	0.18	0.17	0.17	0.20	0.31	0.22	0.25	0.20	0.09	0.11	0.10	0.13	0.42	0.34
Pb	0.27	0.21	0.19	1.58	1.62	1.40	1.81	4.10	2.26	0.27	0.55	0.32	0.54	0.79	1.12
Th	0.05	0.04	0.04	0.05	0.10	0.11	0.08	0.08	0.07	0.01	0.01	0.01	0.02	0.03	0.03
U	0.02	0.02	0.02	0.02	0.04	0.05	0.03	0.03	0.02	0.00	0.01	0.01	0.01	0.02	0.01
Platinum-group elements (ppb)															
Ru	Bdl[c]		Bdl	Bdl		Bdl			Bdl	0.57					0.16
Rh	Bdl		Bdl	Bdl		Bdl			Bdl	0.98					0.48
Pd	0.17		0.08	0.09		0.13			0.15	27.42					5.76
Ir	0.03		0.02	0.02		0.02			0.02	0.50					0.33
Pt	0.03		0.01	0.10		0.05			0.01	29.60					13.48

[a] Measured values of standards (see text for details).
[b] Total iron as Fe_2O_3.
[c] Bdl = below detection limit.

layered gabbros and most pronounced in the Fe-Ti oxide ores (Fig. 9c and d). In general, the PGE contents of the samples are low and follow the order: microgabbros > Fe-Ti oxide ores > layered gabbros > isotropic gabbros (Table 2). The mantle-normalized PGE patterns for different rock types are marked by either flat or negative slopes from Ni to Ru and positive slopes from Ru to Cu (Fig. 10a–d). In addition, the isotropic gabbros and some layered gabbros show negative Ru anomaly, a feature also observed for the high-Ti Emeishan basalts (Qi and Zhou, 2008b; Qi et al., 2008; Song et al., 2009; Wang et al., 2011) (Fig. 10a and c). The wehrlite displays a flat PGE pattern with abundances close to primitive mantle values (Fig. 10c).

The initial Sr isotopic ratios and $\varepsilon_{Nd}(t)$ for eight out of nine analyzed samples range from 0.7044 to 0.7045 and +2.4 to +3.9, respectively (Table 3). These isotopic values are neither correlated with Rb/Sr nor Sm/Nd, which range from 0.002 to 0.006 and 0.29–0.32, respectively. Likewise, the isotopic compositions are not related to abundances of Sr and Nd in the samples. A marked exception is the evolved microgabbro (sample LQ32) that has relatively high $(^{87}Sr/^{86}Sr)_i$ of 0.7055 and low $\varepsilon_{Nd}(t)$ of +0.2. Its Rb/Sr (0.001) is lower and Sm/Nd (0.35) is higher than the above samples. On a $\varepsilon_{Nd}(t)$-$(^{87}Sr/^{86}Sr)_i$ diagram, most data plot in the quadrant of depleted mantle and are consistent with the published Sr-Nd isotopic data for the Panzhihua intrusion (Fig. 11). However, the published data also indicate that some isotopically enriched materials, analogous to that shown by sample LQ32, might have been involved in the petrogenesis of the intrusion.

Layered gabbro						Fe-Ti oxide ore						Wehrlite	Reference materials[a]			
LQ37	LQ42	LQ43	LQ44	LQ50	LQ52	LQ19	LQ20	LQ22	LQ23	LQ24	LQ35	LQ47	MSAN	OU-6	AMH-1	WPR-1
Major oxides (wt.%)																
25.60	31.82	37.96	29.19	26.89	31.83	15.28	12.49	13.42	5.08	10.71	15.30	38.13				
8.35	6.51	4.78	8.99	10.59	11.09	11.13	12.23	12.91	15.63	14.27	10.45	2.29				
7.69	8.64	11.14	6.78	8.77	8.86	6.36	4.12	4.29	4.04	3.88	5.44	4.22				
44.16	31.83	22.11	32.39	36.05	28.10	58.71	63.45	63.95	73.00	67.73	59.07	17.23				
0.30	0.22	0.19	0.24	0.24	0.22	0.25	0.22	0.21	0.23	0.22	0.22	0.25				
5.86	7.81	7.56	7.89	6.26	6.91	3.35	3.09	2.96	2.37	2.75	3.46	22.66				
5.94	10.22	12.40	10.41	7.83	9.38	1.65	1.36	1.54	0.09	0.60	2.28	8.54				
0.63	1.16	1.69	0.75	1.62	2.00	0.36	0.20	0.21	0.02	0.19	0.34	0.32				
0.05	0.12	0.09	0.03	0.12	0.10	0.04	0.02	0.02	0.00	0.02	0.04	0.03				
0.01	0.00	0.00	0.00	0.00	0.00	0.00	0.00	0.00	0.00	0.00	0.00	0.00				
–	0.23	0.67	1.40	–	0.13	–	–	–	–	–	–	5.56				
		0.51		0.83	0.67	5.63	2.32	1.94	1.04	0.74		0.42				
1.29	2.67	1.49	0.75	1.44	1.48	0.76	0.42	0.65	0.05	0.67	0.87	0.49	19.2	99.9	11.6	
26.7	28.7	30.8	30.6	23.8	28.4	10.4	14.0	15.6	10.4	12.0	14.1	26.1	22.6	23.1	14.1	
1875	702	649	810	885	656	2792	3179	3354	3947	3736	3048	192	197	130	108	
52.7	21.7	12.8	38.0	151.9	11.4	260	272	271	407	422	237	1349	81.2	67.7	39.4	
182	147	102	141	156	126	202	212	252	225	229	248	117	24.9	30.9	20.1	
77.4	146	36.2	71.2	43.6	33.9	171	167	163	172	159	125	704	35.5	39.1	33.7	
95.4	629	54.8	87.5	87.8	62.7	362	252	196	279	219	238	13.0	54.1	42.6	30.0	
258	208	156	195	266	182	383	405	388	461	448	352	130	90.1	121	71.3	
28.5	23.5	21.7	19.2	25.4	20.3	37.4	36.4	37.9	38.1	39.9	36.3	9.89	18.0	25.9	20.2	
0.57	1.20	1.25	0.71	1.25	1.06	0.61	0.35	0.46	0.26	0.43	1.09	0.81	33.2	133	20.4	
167	307	436	255	390	413	181	71.2	120	12.9	86.8	178	101	373	141	559	
5.87	7.24	7.93	7.05	4.43	5.69	0.48	1.29	1.42	0.16	0.50	1.75	8.56	27.7	27.2	14.7	
20.4	29.4	20.8	23.7	21.1	34.5	16.9	20.4	22.5	22.5	21.6	17.7	25.6	142	185	141	
1.91	2.80	1.52	3.02	3.82	10.14	2.98	3.19	3.48	4.05	3.74	2.56	1.76	6.18	14.5	8.05	
0.04	0.06	0.11	0.11	0.10	0.09	0.04	0.03	0.03	0.03	0.05	0.04	0.06	1.64	8.17	0.29	
21.4	62.1	50.8	16.7	49.3	54.6	21.9	10.2	16.1	3.27	13.1	23.6	9.4	260	498	320	
1.18	2.05	1.93	1.36	1.09	1.48	0.44	0.49	0.62	0.15	0.45	0.68	1.25	16.5	34.8	17.0	
3.91	6.01	5.97	4.37	3.07	4.25	0.89	1.25	1.56	0.33	0.99	1.72	4.28	34.6	81.4	33.7	
0.76	1.13	1.05	0.83	0.59	0.74	0.11	0.21	0.25	0.05	0.14	0.29	0.92	4.99	8.61	4.46	
4.26	6.02	6.26	5.14	3.33	4.08	0.53	1.12	1.24	0.18	0.57	1.48	5.68	20.9	31.8	17.3	
1.39	1.83	1.79	1.72	1.02	1.27	0.08	0.26	0.33	Bdl[c]	0.12	0.42	1.93	4.80	6.28	3.72	
0.60	0.80	0.89	0.77	0.57	0.73	0.14	0.16	0.18	0.02	0.08	0.23	0.76	1.39	1.37	1.16	
1.65	1.91	2.20	2.07	1.24	1.63	0.21	0.46	0.43	0.13	0.22	0.57	2.17	4.91	5.51	3.42	
0.25	0.30	0.33	0.30	0.18	0.23	0.02	0.05	0.06	0.00	0.02	0.07	0.34	0.81	0.94	0.52	
1.33	1.60	1.67	1.60	0.96	1.23	0.06	0.27	0.28	0.02	0.10	0.41	1.90	4.68	5.04	2.68	
0.26	0.31	0.33	0.30	0.19	0.23	0.02	0.06	0.06	0.01	0.01	0.08	0.37	1.02	1.12	0.56	
0.64	0.77	0.87	0.74	0.47	0.59	0.04	0.15	0.16	0.02	0.05	0.20	0.93	3.06	3.26	1.61	
0.08	0.09	0.09	0.09	0.06	0.07	0.01	0.02	0.02	0.00	0.01	0.02	0.11	0.40	0.46	0.22	
0.43	0.55	0.52	0.52	0.36	0.48	0.04	0.09	0.12	0.02	0.04	0.14	0.65	2.89	3.19	1.42	
0.06	0.07	0.09	0.07	0.05	0.06	0.01	0.01	0.02	0.00	0.01	0.02	0.09	0.40	0.50	0.22	
0.85	1.11	0.90	1.03	0.85	1.23	0.64	0.78	0.81	0.77	0.81	0.65	1.07	3.83	4.98	3.90	
0.19	0.26	0.14	0.32	0.50	1.01	0.29	0.30	0.33	0.39	0.38	0.27	0.20	0.58	1.04	0.60	
0.45	3.03	0.38	0.52	0.15	0.23	1.48	1.49	2.51	1.32	2.54	2.28	0.19	18.3	31.0	9.04	
0.05	0.07	0.07	0.05	0.04	0.06	0.02	0.04	0.05	0.02	0.04	0.04	0.03	3.45	11.2	2.54	
0.02	0.02	0.02	0.01	0.02	0.02	0.01	0.01	0.02	0.02	0.02	0.02	0.01	1.40	2.17	0.89	
		0.01		0.19	0.01	0.19	0.13	0.16	0.22	0.26		3.08				21.8
		0.03		0.19	0.03	0.10	0.20	0.25	0.28	0.29		0.93				12.3
		1.00		3.20	0.57	4.53	4.82	7.18	5.49	6.37		1.59				235.3
		0.03		0.07	0.04	0.10	0.12	0.12	0.14	0.17		1.80				14.3
		1.17		3.84	0.80	3.35	4.25	6.79	5.23	5.50		14.30				274.4

5.2. Stratigraphic variations

The stratigraphic variations of mineral compositions and bulk-rock geochemical and Sr-Nd isotopic data are illustrated in Fig. 12. As expected from the above results, An content of plagioclase and $Mg^{\#}$ of clinopyroxene vary in a limited manner over the studied section except the evolved microgabbro at ~15 m level (Fig. 12a and b). Vanadium and Cr display large variations and parallel trends over the section; their concentrations are low in the isotropic gabbros and are higher in the overlying rocks (Fig. 12c and d). The Ti/V of clinopyroxene is relatively uniform over the section but the bulk-rock Ti/V is variable (Fig. 12e and f); the isotropic gabbros have Ti/V of ~50–500 whereas most overlying rocks have Ti/V of ~70 or less. The La/Yb and Ba/Y values increase upwards in the isotropic gabbro and decrease abruptly to low values in the overlying rocks (Fig. 12g and h). The Cu/Pd is extremely high in the isotropic gabbros (~360,000–2,200,000) and its value decreases in the overlying rocks (~110,000 or below) (Fig. 12i). As expected, $\varepsilon_{Nd}(t)$ does not show large variations over the section except the evolved microgabbro (Fig. 12j).

6. Discussion

6.1. Effect of cumulus titanomagnetite on trace element fractionation

When arranged according to relative incompatibility, the HFSE and REE should show parallel behavior and thus smooth

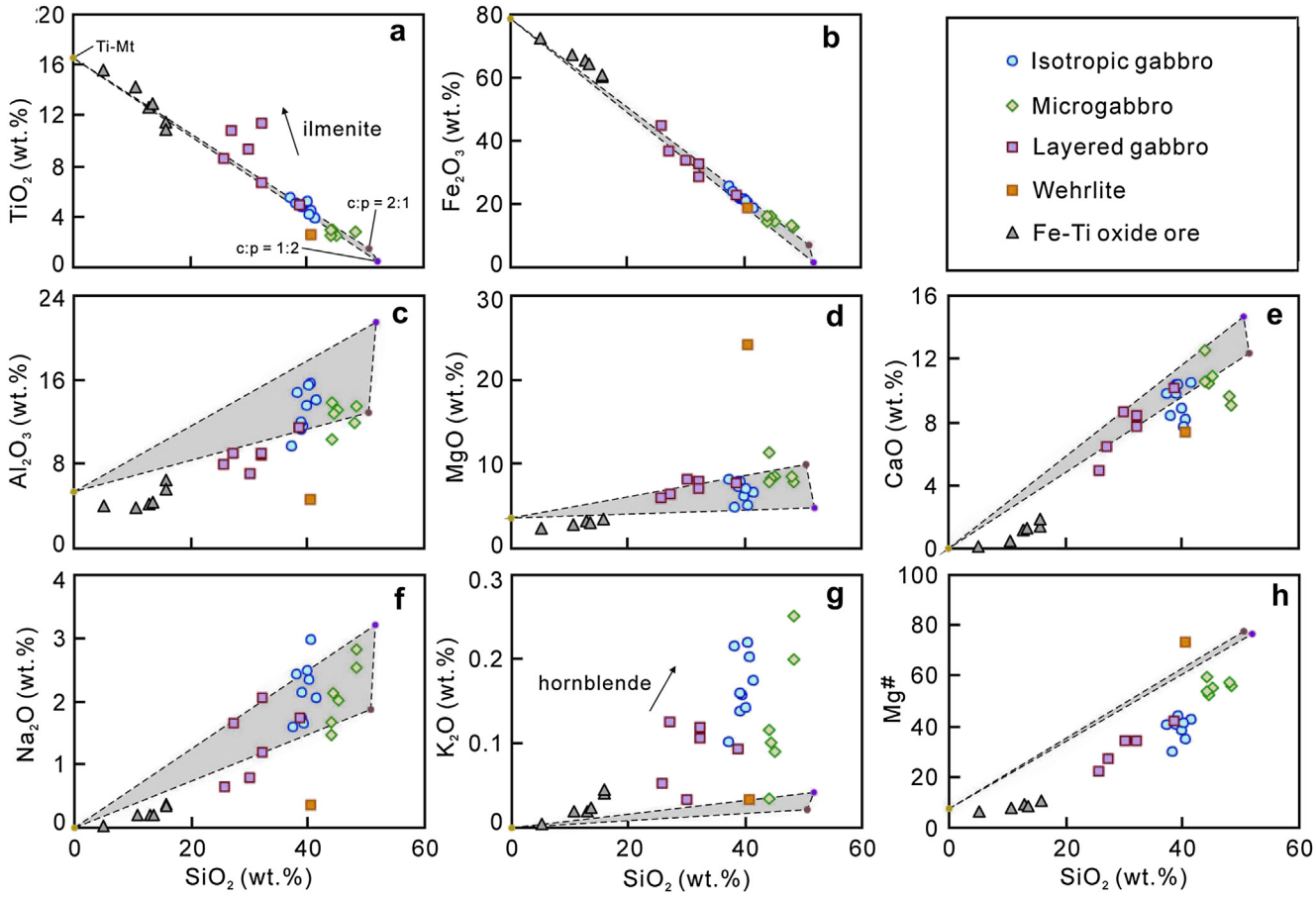

Figure 6. Concentrations of major element oxides and $Mg^{\#}$ versus SiO_2 in rocks from the studied section at Nalaqing. a: TiO_2. b: Fe_2O_3. c: Al_2O_3. d: MgO. e: CaO. f: Na_2O. g: K_2O. h: $Mg^{\#}$. Gray fields bounded by dashed lines are plotted with reference to a melanogabbroic pole (clinopyroxene:plagioclase = 2:1), a leucogabbroic pole (clinopyroxene:plagioclase = 1:2) and the primary titanomagnetite composition estimated by Pang et al. (2008a). The clinopyroxene ($Mg^{\#}$ = 78) and plagioclase (An_{60}) used are average values of the studied section (Table 1 and Fig. 5a).

patterns on primitive mantle- or MORB-normalized diagrams. Trace element patterns associated with large troughs or spikes, which indicate strong fractionation of elements with similar incompatibilities, have to be explained by processes other than mantle melting, fractionation or accumulation of crystals commonly present in mafic–ultramafic magmas. As described above, the layered gabbros and Fe-Ti oxide ores exhibit strong fractionation between HFSE and REE (Fig. 9c and d). In the following discussion, we examine this unusual geochemical feature.

Fig. 9 shows three important features with respect to the fractionation between HFSE and REE: (i) all samples exhibit positive Ti anomaly and it is stronger in the layered gabbros and Fe-Ti oxide ores than the isotropic gabbros and microgabbros, (ii) the layered gabbros and oxide ores display large negative La anomaly (relative to Nb and Ta), which is only weakly developed in the isotropic gabbros and microgabbros, and (iii) the oxide ores show positive Zr-Hf anomalies relative to Nd and Sm. To explain these features, either fractionation (or equilibration) of a phase in which REE is preferentially partitioned over HFSE, or accumulation of a phase with the reversed behavior (i.e. high HFSE/REE), is required. The apatite-melt partition coefficients for the REE are known to be much higher than for the HFSE and thus apatite fractionation might be able to cause substantial HFSE-REE decoupling (Prowatke and Klemme, 2006). In the Panzhihua intrusion, however, cumulus apatite is only present at higher stratigraphy (MZb) than the Nalaqing section (near the LZ–MZa transition) (Fig. 2) and there is no evidence to suggest any substantial apatite fractionation occurred prior to emplacement of the intrusion. The variable HFSE-REE decoupling in different rock types is also inconsistent with explanation involving apatite fractionation.

The preferential incorporation of HFSE in magnetite and ilmenite is well-known and experimentally demonstrated (Nielsen et al., 1994; Nielsen and Beard, 2000; Klemme et al., 2006), presumably substituting for Ti in the oxide crystal lattice. In contrast, this effect is not known for REE, at least not at comparable extents as the HFSE. The fact that significant accumulation of Fe-Ti oxides occurred in the Panzhihua intrusion is inescapable (Ganino et al., 2008; Pang et al., 2008a,b; Zhang et al., 2009) and thus their variable abundances most likely explain the fractionation between HFSE and REE. To further quantify this effect, we introduce the variable Ti/Ti^* as a measure of the degree of Ti anomaly relative to Eu and Gd (Ti^* is the amount of Ti inferred from the mantle-normalized abundances of Eu and Gd). A value of 1 means that Ti is not anomalous; values greater than 1 and less than 1 denote positive and negative Ti anomalies, respectively. Positive correlations between Nb/La, Hf/Sm and Ti/Ti^* shown by our data and published data for the Panzhihua intrusion suggest that the degree of HFSE-REE decoupling is related to the amount of

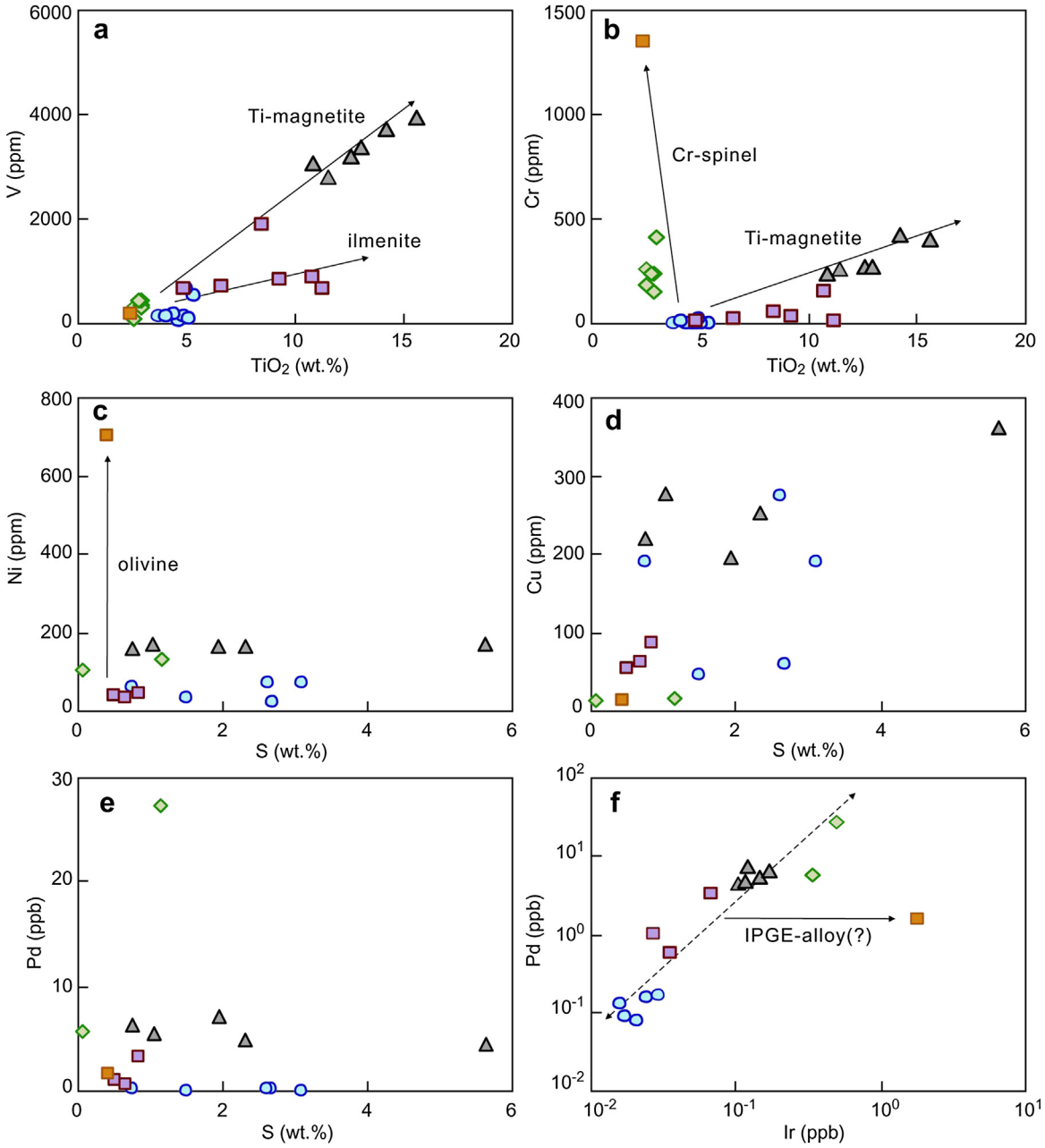

Figure 7. Binary diagrams illustrating the control of selected trace elements in rocks from the studied section at Nalaqing. a: V versus TiO_2. b: Cr versus TiO_2. c: Ni versus S. d: Cu versus S. e: Pd versus S. f: Pd versus Ir. Legend is the same as in Fig. 6.

Fe-Ti oxides present in the rocks (Fig. 13a and b). Based on the above arguments, we suggest that variable accumulation of Fe-Ti oxides at relatively low trapped liquid contents provides the best explanation for the fractionation between HFSE and REE in the studied samples.

6.2. Origin of texturally distinctive gabbros

The lack of layered structure in the lower part of the Panzhihua intrusion is noted by previous workers (Pang et al., 2008a, 2009; Hou et al., 2012b). Apart from a general isotropic and coarse-grained appearance, gabbros therein also contain pegmatitic pods, lenses and dykes, the development of which tends to become more intense toward the intrusive contact. Such pegmatitic pods are also observed in the isotropic gabbros of the studied section (Fig. 4a). Genesis of pegmatites is generally favored under fluid-rich conditions (Beard and Day, 1986). If this is correct, the formation of isotropic gabbros might be related to fluxing of CO_2-rich fluid released from the country rocks (Ganino et al., 2008).

The next question is how the isotropic gabbros are related to the overlying rocks. Here, our textural observations and geochemical data provide a basic framework for the interpretation of the origin of the isotropic and layered gabbros, which is summarized as follows:

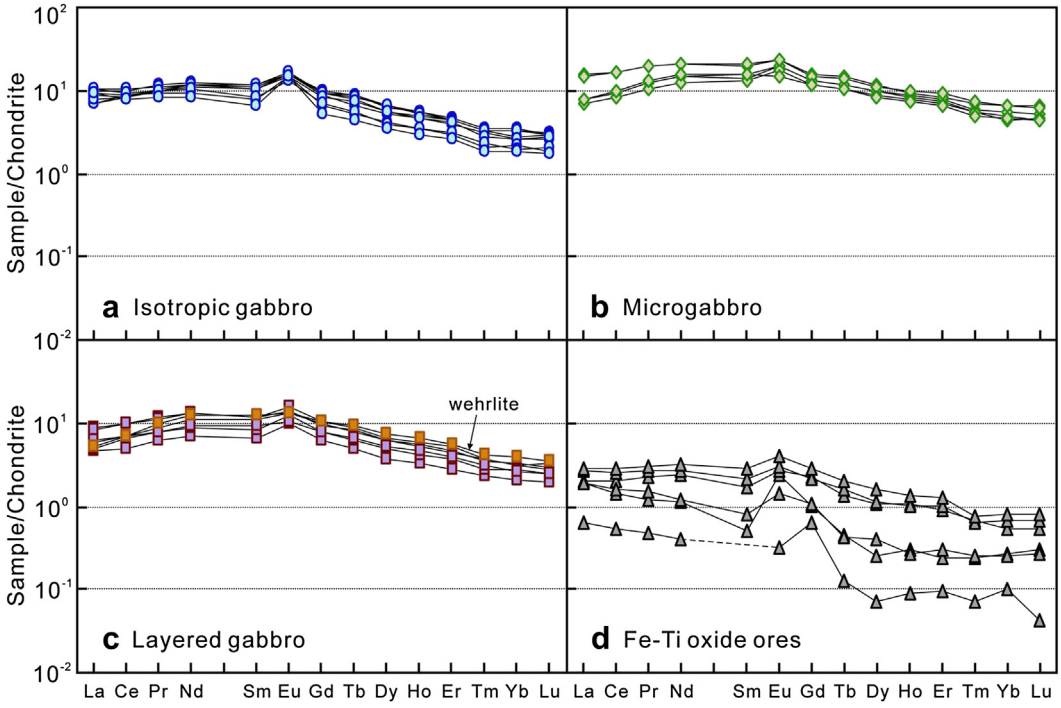

Figure 8. Chondrite-normalized REE diagrams for rocks from the studied section at Nalaqing. a: Isotropic gabbros. b: Microgabbros. c: Layered gabbros. d: Fe-Ti oxide ores. Normalizing values are after Sun and McDonough (1989).

(i) Both the isotropic and layered gabbros are cumulates as shown by textures and low abundances of incompatible trace elements.
(ii) They have overlapping and largely uniform mineral compositions (An of plagioclase, $Mg^{\#}$ of clinopyroxene), indicating formation from a common magma or magma(s) at similar degrees of differentiation.
(iii) They have similar Sr-Nd isotopic compositions suggestive of crystallization from a common magma or batches of magma derived from a similar source.

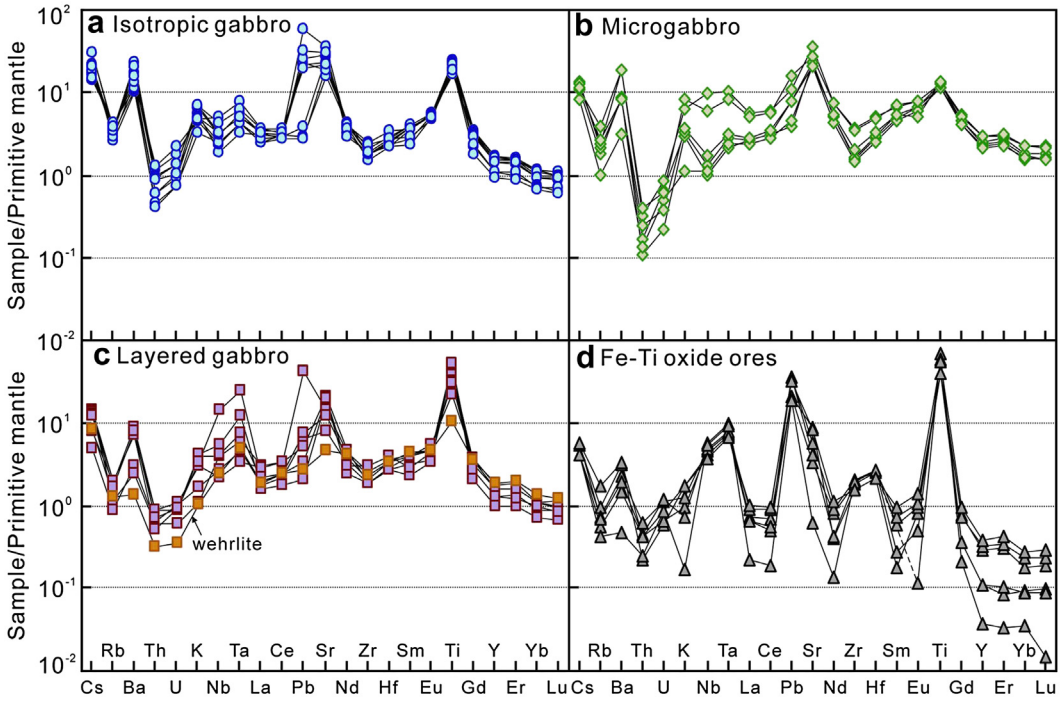

Figure 9. Primitive mantle-normalized trace element diagrams for rocks from the studied section at Nalaqing. a: Isotropic gabbros. b: Microgabbros. c: Layered gabbros. d: Fe-Ti oxide ores. Normalizing values are after Sun and McDonough (1989).

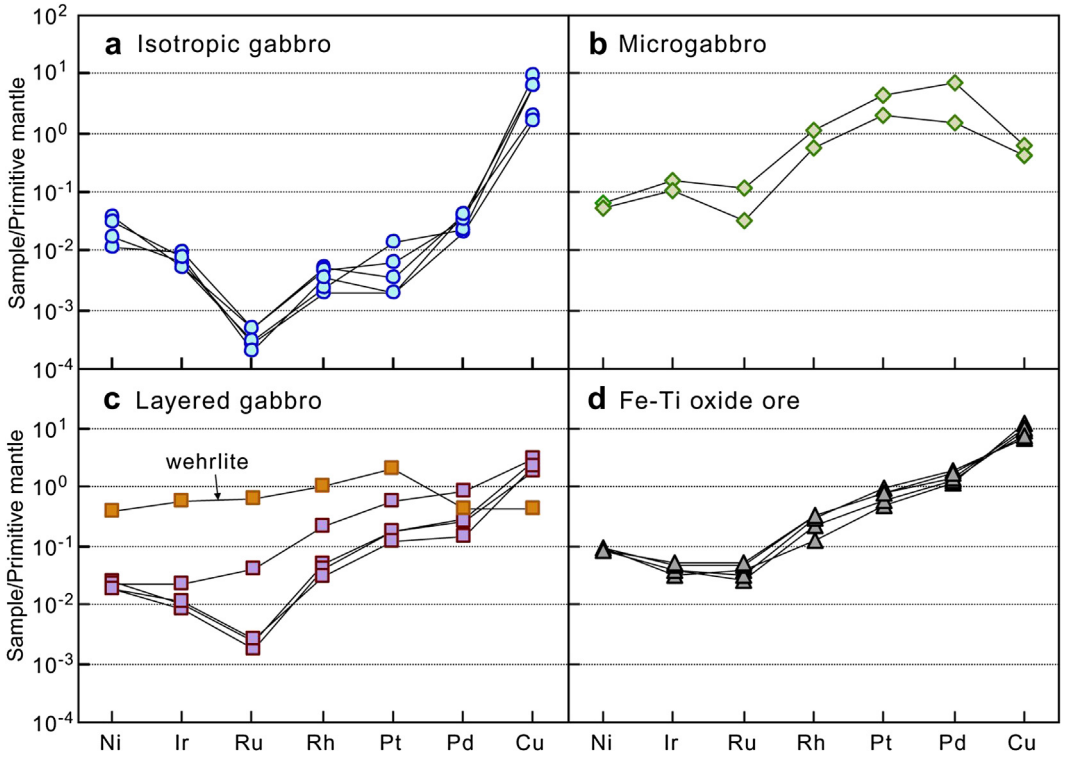

Figure 10. Primitive mantle-normalized chalcophile element diagrams for rocks from the studied section at Nalaqing. a: Isotropic gabbros. b: Microgabbros. c: Layered gabbros. d: Fe-Ti oxide ores. Normalizing values are after McDonough and Sun (1995).

In view of the above, one simple interpretation is that the isotropic and layered gabbros are cumulates crystallized from a common differentiating magma at a similar time. The formation of medium-grained layered gabbros possibly reflects a diminishing effect of fluid fluxing and layered formation was favored. As elaborated below, however, the above interpretation fails to explain some other geochemical features and might have been over-simplified.

The isotropic gabbros are very poor in V and Cr compared to the overlying layered gabbros by differences up to an order of magnitude (Figs. 7a, b and 12d, e), which seem too large to be solely ascribed to variable abundances of Fe-Ti oxides. To illustrate this, we computed the Ti/V values for both bulk-rock and clinopyroxene over the studied section (Fig. 12e and f). The isotropic gabbros have much higher bulk-rock Ti/V than the layered gabbros, whereas the Ti/V in clinopyroxene from both rock types is similar. This indicates that (i) the bulk-rock Ti and V abundances are mainly controlled by Fe-Ti oxides, and (ii) Fe-Ti oxides in the isotropic gabbros are low in V and Cr, and high in Ti/V, compared to those in the overlying layered gabbros.

Table 3
Sr-Nd isotopic data for rocks from the studied section at Nalaqing.

	Rb (ppm)	Sr (ppm)	$^{87}Rb/^{86}Sr$	$^{87}Sr/^{86}Sr$	$\pm2\sigma_m$	$(^{87}Sr/^{86}Sr)_i$	Sm (ppm)	Nd (ppm)	$^{147}Sm/^{144}Nd$	$^{143}Nd/^{144}Nd$	$\pm2\sigma_m$	$(^{143}Nd/^{144}Nd)_i$	$\varepsilon_{Nd}(t)$
Isotropic gabbro													
LQ03	1.67	338	0.014	0.704475	11	0.7044	1.78	5.56	0.194	0.512781	2	0.5125	2.9
LQ07	2.75	481	0.017	0.704484	9	0.7044	1.73	5.61	0.186	0.512785	3	0.5125	3.2
LQ11	1.81	468	0.011	0.704533	7	0.7045	1.59	5.54	0.174	0.512742	3	0.5124	2.8
Microgabbro													
LQ17	1.13	478	0.007	0.704472	10	0.7044	2.19	6.84	0.193	0.512831	4	0.5125	3.9
LQA8	1.52	570	0.008	0.704539	9	0.7045	3.12	9.88	0.191	0.512830	4	0.5125	3.9
LQ32	0.62	447	0.004	0.705559	6	0.7055	2.02	5.70	0.214	0.512681	4	0.5123	0.2
Layered gabbro													
LQ42	1.20	307	0.011	0.704544	8	0.7045	1.83	6.02	0.184	0.512742	5	0.5124	2.5
LQ43	1.25	436	0.008	0.704495	12	0.7045	1.79	6.26	0.173	0.512794	4	0.5125	3.8
LQ52	1.06	413	0.007	0.704535	11	0.7045	1.27	4.08	0.188	0.512748	5	0.5124	2.4

The elemental data were obtained by ICP-MS. $(^{87}Sr/^{86}Sr)_i$ and ε_{Nd} are calculated based on t = 260 Ma, decay constants $\lambda(^{87}Rb) = 1.42 \times 10^{-11}$ year^{-1} and $\lambda(^{147}Sm) = 6.54 \times 10^{-12}$ year^{-1}, and present-day chondritic uniform reservoir values of $^{87}Rb/^{86}Sr = 0.0827$, $^{147}Sm/^{144}Nd = 0.1967$, $^{87}Sr/^{86}Sr = 0.7045$ and $^{143}Nd/^{144}Nd = 0.512638$ (Faure and Mensing, 2005).

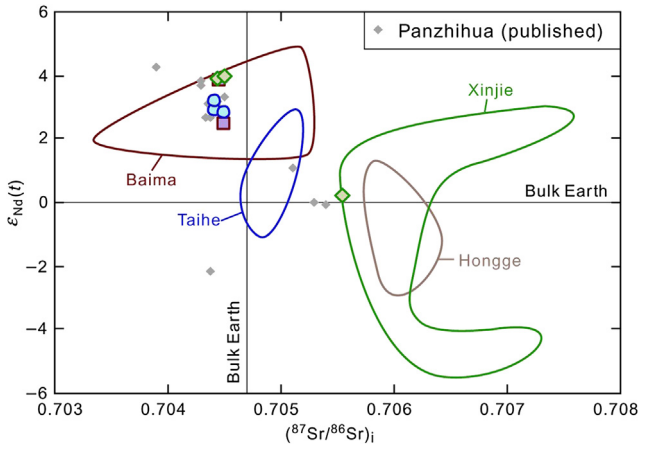

Figure 11. A binary diagram of $\varepsilon_{Nd}(t)$ versus $(^{87}Sr/^{86}Sr)_i$ for rocks from the studied section at Nalaqing. The isotopic data were calculated at $t = 260$ Ma (see footnote of Table 3). Gray diamonds denote published data by Zhou et al. (2008) and Zhang et al. (2009). Reference fields for the isotopic composition of other Fe-Ti oxide ore-bearing intrusions are shown for comparison (after Pang et al., 2010; Hou et al., 2012a). Legend is the same as in Fig. 6.

Further, there are considerable differences in La/Yb, Ba/Y and Cu/Pd between the two types of gabbros, especially at the transition between them (Fig. 12g–i). These ratios do not involve HFSE and should not be affected by titanomagnetite accumulation (see earlier discussion). Both La/Yb and Ba/Y are controlled by silicate phases; La and Ba are highly incompatible whereas Yb and Y are moderately incompatible. Palladium and Cu are compatible in sulfides but incompatible in all common minerals that crystallize in mafic magmas. Under closed-system conditions, the Cu/Pd of a melt could only evolve toward constant (S-undersaturated) or very high values (S-saturated) (Barnes et al., 1993; Mungall, 2005 and references therein). As shown in Fig. 12, however, Cu/Pd drops from very high values in the isotropic gabbros to the overlying rocks, and thus cannot be explained by closed system magma differentiation, whether S-saturated or not. In summary, the above trace element trends are not consistent with closed-system differentiation of a common magma.

The microgabbros show fine-grained and equigranular textures consistent with rapid nucleation and cooling (Fig. 4h). Its concordance with the layered gabbros and Fe-Ti oxide ore horizons, together with the absence of quenched tops and bottoms, argue against injection at a late-stage after solidification of the isotropic and layered gabbros. However, the microgabbros have relatively low trace element abundances,

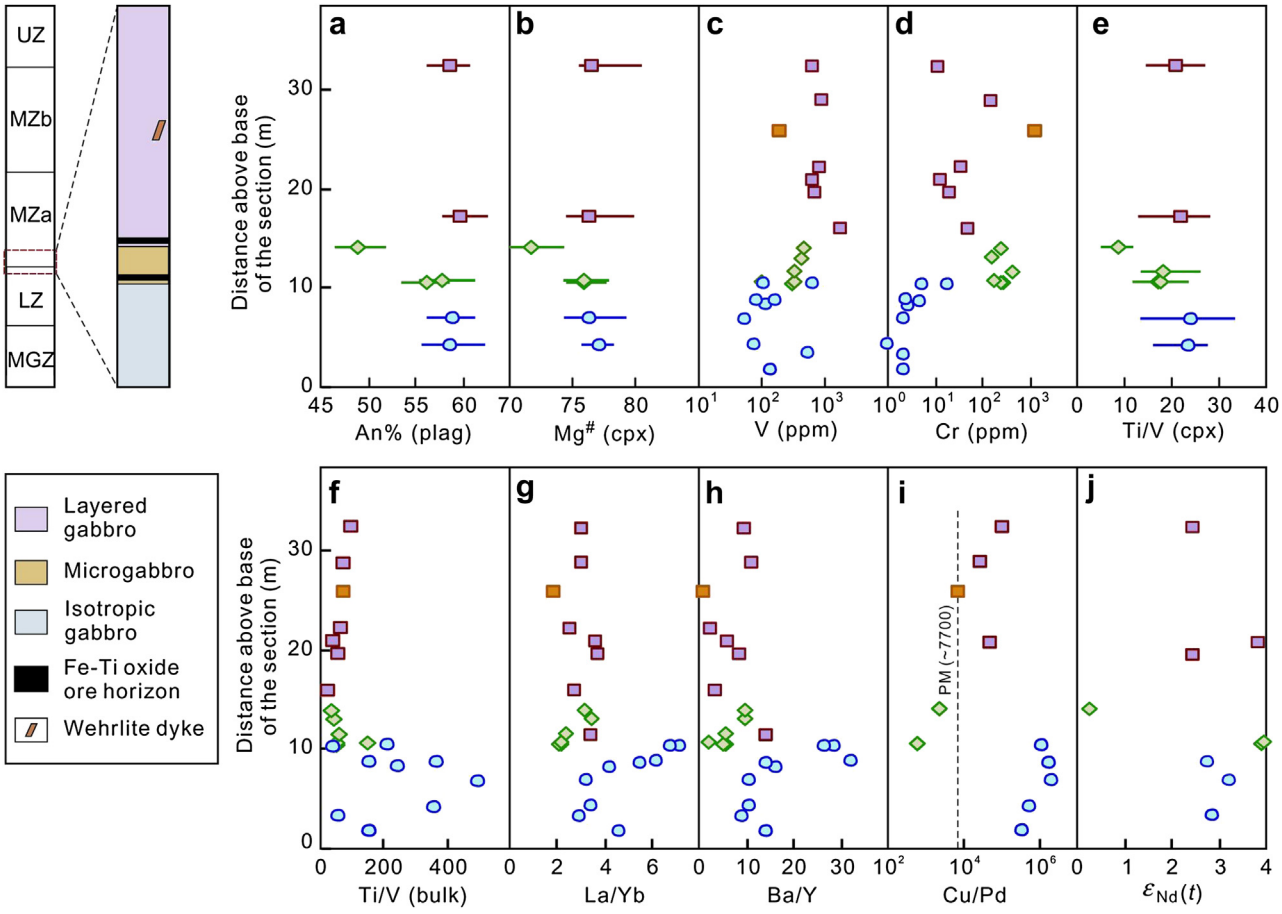

Figure 12. Mineral compositional, geochemical and Nd isotopic variations of the studied section at Nalaqing. a: An of plagioclase. b: $Mg^{\#}$ of clinopyroxene. c: V. d: Cr. e: Ti/V of clinopyroxene. f: Bulk-rock Ti/V. g: La/Yb. h: Ba/Y. i: Cu/Pd. j: $\varepsilon_{Nd}(t)$. Color scheme of the section follows the lower frame of Fig. 3. Data for the Fe-Ti oxide ores are not plotted. Legend is the same as in Fig. 6.

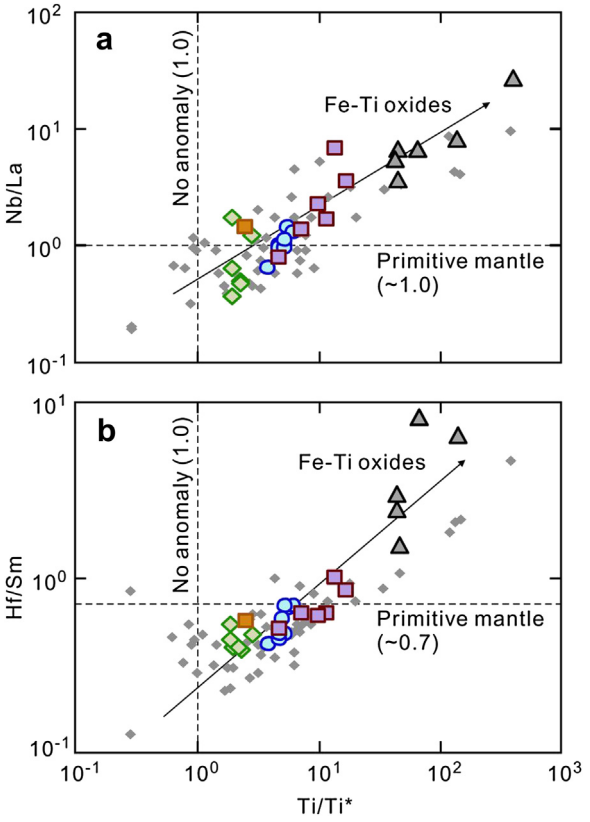

Figure 13. Binary diagrams showing the effect of cumulus Fe-Ti oxides on the fractionation between HFSE and REE. a: Nb/La versus Ti/Ti*. b: Hf/Sm versus Ti/Ti*. Ti/Ti* is a measure of the strength of Ti anomaly in trace element patterns and $Ti^* = (Eu_N + Gd_N)/2$ where the subscript N denotes primitive mantle-normalized elemental abundance.

suggesting some lost of residual liquid was inevitable despite rapid nucleation and cooling. Thus, the microgabbros might not represent an intraplutonic quench zone *sensu stricto* (Tegner et al., 1993), but this does not preclude them from being related to magma addition. In fact, the available data show that plagioclase composition changes from ~An_{60} to ~An_{70} over a >100 m vertical interval in the lower MZa of the Panzhihua intrusion (see Fig. 8c in Pang et al., 2009), implying that magma addition might not be as abrupt as generally appreciated in this particular case. In view of the above arguments, we speculate that the formation of microgabbros might be associated with the onset of successive magma recharge events, which eventually led to the crystallization of plagioclase with ~An_{70} in the middle MZa.

6.3. Implications for differentiation and Fe-Ti oxide ore genesis

Our data, together with available data and observations, allow us to propose a model for the formation of the lower parts of the Panzhihua intrusion. The parental ferrobasaltic magma was emplaced in the Panzhihua chamber. As a result of contact metamorphism, CO_2-rich fluid was released from the carbonate wall-rocks into the solidification zone of the magma and increased its $f(O_2)$ (see Ganino et al., 2008) (Fig. 14a). This triggered abundant crystallization of titanomagnetite and formation of coarse-grained isotropic gabbros in a relatively dynamic environment due to elevated fluid content. At this stage, the magma underwent in-situ crystallization (see Langmuir, 1989) and hence very limited fractionation, resulting in largely uniform plagioclase composition (Fig. 14a). After the LZ cumulates reached a certain thickness, the effect of CO_2 release was lessened, igneous layering started to develop in a relatively static environment and the ore horizons formed at this stage were much less extensive (Fig. 14b). At this stage, successive magma addition resulted in increasing An of plagioclase upwards. From the middle MZa upwards, the magma evolved by largely closed-system fractionation, causing gradual decrease in An of plagioclase upwards (Fig. 14c). No Fe-Ti oxide ore horizons formed at this stage except disseminated oxides in gabbroic cumulates. If this model is correct, then the Panzhihua magma chamber might possess some open system behavior (i.e. periodically replenished and tapped), and the Fe-Ti oxide ores therein might have formed from a larger volume of magma than is now preserved in the intrusion. Another important inference derived from the model is that the increasing scale and abundance of Fe-Ti oxide ores in the lower part of the intrusion might reflect the availability of CO_2 from the country rocks that triggered ore formation, in addition to settling and sorting of dense titanomagnetite in magma (Pang et al., 2008a).

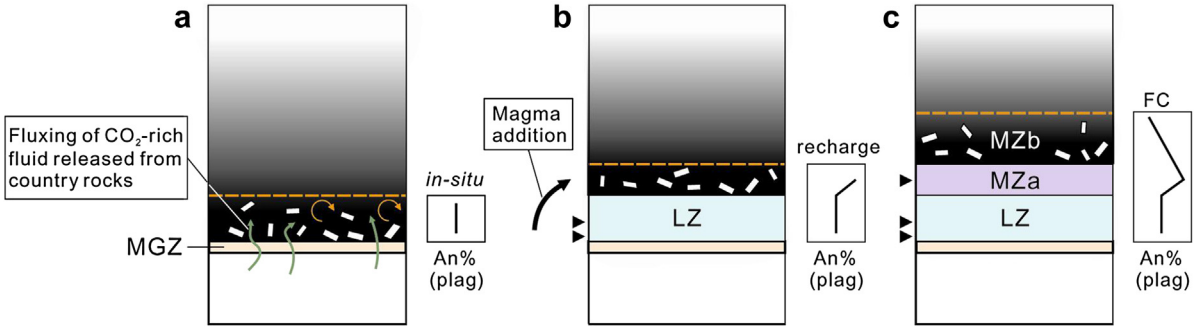

Figure 14. A model for the formation of the lower parts of the Panzhihua intrusion. a: In-situ stage involving fluxing of CO_2-rich fluid from the carbonate country rocks and formation of abundant Fe-Ti oxide ores in a relatively dynamic environment (black triangles). b: Recharge stage involving successive addition of magma batches after partial solidification of the LZ and formation of less extensive oxide ore horizons in a relatively static environment; igneous layering is well-developed starting from this stage. c: Fractionation stage involving largely closed system fractional crystallization and formation of layered gabbros and leucogabbros in the upper MZa and MZb; ore formation is less favorable at this stage and the Fe-Ti oxides are disseminated in the gabbros.

7. Conclusions

The conclusions of this study are summarized below:

(1) Isotropic and layered gabbros in the Nalaqing mine at the southern tip of the Panzhihua intrusion are cumulates and are likely cogenetic, as indicated by similar plagioclase and clinopyroxene compositions, and Sr-Nd isotopic composition.
(2) The two types of gabbros exhibit marked variations in Cr, V, PGE, Ti/V, La/Yb, Ba/Y and Cu/Pd, features that are difficult to explain by cumulate formation from a common magma in a closed system.
(3) Microgabbros separating the isotropic and layered gabbros have similar major element compositions as the high-Ti Emeishan basalts, but their low trace element abundances indicate that some lost of residual liquid was inevitable despite rapid nucleation and cooling.
(4) The formation of texturally distinctive gabbros at Nalaqing can be explained by changing crystallization conditions associated with the onset of successive magma recharge at the transition between the LZ and MZa.
(5) Strong decoupling between HFSE and REE in a subset of samples is caused by the accumulation of titanomagnetite.

Acknowledgments

We thank Jun-Hong Zhao for field assistance, Chusi Li for electron microprobe analyses, and Xiao Fu and Jian-Feng Gao for XRF measurements. This study is supported by the Research Grant Council of Hong Kong (HKU707012P) to MFZ and a post-doctoral fellowship awarded by the National Science Council (NSC), Taiwan to KNP.

References

Anh, T.V., Pang, K.-N., Chung, S.-L., Lin, H.-M., Tran, T.H., Tran, T.A., Yang, H.-J., 2011. The Song Da magmatic suite revisited: a petrologic, geochemical and Sr–Nd isotopic study on picrites, flood basalts and silicic volcanic rocks. Journal of Asian Earth Sciences 42, 1341–1355.

Bai, Z.-J., Zhong, H., Naldrett, A.J., Zhu, W.-G., Xu, G.-W., 2012. Whole-rock and mineral composition constraints on the genesis of the giant Hongge Fe–Ti–V oxide deposit in the Emeishan large igneous province, southwest China. Economic Geology 107, 507–524.

Barnes, S.-J., Couture, J.-F., Sawyer, E.W., Bouchaib, C., 1993. Nickel–copper occurrences in the Belleterre–Angliers belt of the Pontiac subprovince and the use of Cu–Pd ratios in interpreting platinum-group element distributions. Economic Geology 88, 1402–1419.

Beard, J.S., Day, H.W., 1986. Origin of gabbro pegmatite in the Smartville intrusive complex, northern Sierra Nevada, California. American Mineralogist 71, 1085–1099.

Chung, S.-L., Jahn, B.-M., 1995. Plume–lithosphere interaction in generation of the Emeishan flood basalts at the Permian–Triassic boundary. Geology 23, 889–892.

Chung, S.-L., Jahn, B.-M., Wu, G.-Y., Lo, C.-H., Cong, B.-L., 1998. The Emeishan flood basalt in SW China: a mantle plume initiation model and its connection with continental breakup and mass extinction at the Permian–Triassic boundary. In: Flower, M.F.J., Chung, S.-L., Lo, C.-H., Lee, T.-Y. (Eds.), Mantle Dynamics and Plate Interactions in East Asia. Geodynamics Series, vol. 27. American Geophysical Union, Washington, pp. 47–58.

Faure, G., Mensing, T.M., 2005. Isotopes: Principles and Applications. John Wiley and Sons, New Jersey.

Ganino, C., Arndt, N.T., Zhou, M.-F., Gaillard, F., Chauvel, C., 2008. Interaction of magma with sedimentary wall rock and magnetite ore genesis in the Panzhihua mafic intrusion, SW China. Mineralium Deposita 43, 677–694.

Hou, T., Zhang, Z., Ye, X., Encarnacion, J., Reichow, M.K., 2011. Noble gas isotopic systematics of Fe–Ti–V oxide ore-related mafic-ultramafic layered intrusions in the Panxi area, China: the role of recycled oceanic crust in their petrogenesis. Geochimica et Cosmochimica Acta 75, 6727–6741.

Hou, T., Zhang, Z., Encarnacion, J., Santosh, M., 2012a. Petrogenesis and metallogenesis of the Taihe gabbroic intrusion associated with Fe–Ti-oxide ores in the Panxi district, Emeishan large igneous province, southwest China. Ore Geology Reviews 49, 109–127.

Hou, T., Zhang, Z., Pirajno, F., 2012b. A new metallogenic model of the Panzhihua giant V–-Ti–iron oxide deposit (Emeishan large igneous province) based on high-Mg olivine-bearing wehrlite and new field evidence. International Geology Review 54, 1721–1745.

Irvine, T.N., 1982. Terminology for layered intrusions. Journal of Petrology 23, 127–162.

Klemme, S., Günther, D., Hametner, K., Prowatke, S., Zack, T., 2006. The partitioning of trace elements between ilmenite, ulvospinel, armalcolite and silicate melts with implications for the early differentiation of the moon. Chemical Geology 234, 251–263.

Langmuir, C.H., 1989. Geochemical consequences of in situ crystallization. Nature 340, 199–205.

Lee, H.-Y., Chung, S.-L., Ji, J., Qian, Q., Gallet, S., Lo, C.-H., Lee, T.-Y., Zhang, Q., 2012. Geochemical and Sr–Nd isotopic constraints on the genesis of the Cenozoic Linzizong volcanic successions, southern Tibet. Journal of Asian Earth Sciences 53, 96–114.

Li, C., Tao, Y., Qi, L., Ripley, E.M., 2012. Controls on PGE fractionation in the Emeishan picrites and basalts: constraints from integrated lithosphile–siderophile elements and Sr–Nd isotopes. Geochimica et Cosmochimica Acta 90, 12–32.

Ma, Y., Liu, J.F., Wang, H.F., Mao, Y.S., Ji, X.T., Wang, D.K., Yan, Z.Z., 2001. Geology of the Panzhihua Region. Sichuan Science and Technology Press, Chengdu, 367 pp. (in Chinese).

McDonough, W.F., Sun, S.-S., 1995. The composition of the earth. Chemical Geology 120, 223–253.

Mungall, J.E., 2005. Magmatic geochemistry of the PGE. In: Mungall, J.E. (Ed.), Exploration for Deposits of Platinum-group Elements. Mineralogical Association of Canada Short Course Series, vol. 35, pp. 1–34.

Nielsen, R.L., Beard, J.S., 2000. Magnetite-melt HFSE partitioning. Chemical Geology 164, 21–34.

Nielsen, R.L., Forsythe, L.M., Gallahan, W.E., Fisk, M.R., 1994. Major- and trace-element magnetite-melt equilibria. Chemical Geology 117, 167–191.

Pang, K.-N., Li, C., Zhou, M.-F., Ripley, E.M., 2008a. Abundant Fe–Ti oxide inclusions in olivine from the Panzhihua and Hongge layered intrusions, SW China: evidence for early saturation of Fe–Ti oxides in ferrobasaltic magma. Contributions to Mineralogy and Petrology 156, 307–321.

Pang, K.-N., Zhou, M.-F., Lindsley, D.H., Zhao, D., Malpas, J., 2008b. Origin of Fe–Ti oxide ores in mafic intrusions: evidence from the Panzhihua intrusion. Journal of Petrology 49, 295–313.

Pang, K.-N., Li, C., Zhou, M.-F., Ripley, E.M., 2009. Mineral compositional constraints on petrogenesis and ore genesis of the Panzhihua layered gabbroic intrusion, SW China. Lithos 110, 199–214.

Pang, K.-N., Zhou, M.-F., Qi, L., Shellnutt, G., Wang, C.Y., Zhao, D., 2010. Flood basalt-related Fe–Ti oxide deposits in the Emeishan large igneous province, SW China. Lithos 119, 123–136.

Prowatke, S., Klemme, S., 2006. Trace element partitioning between apatite and silicate melts. Geochimica et Cosmochimica Acta 70, 4513–4527.

Qi, L., Hu, J., Gregoire, D.C., 2000. Determination of trace elements in granites by inductively coupled plasma-mass spectrometry. Talanta 51, 507–513.

Qi, L., Zhou, M.F., Wang, C.Y., 2004. Determination of low concentrations of platinum group elements in geological samples by ID-ICP-MS. Journal of Analytical Atomic Spectrometry 19, 1335–1339.

Qi, L., Zhou, M.F., Wang, C.Y., Sun, M., 2007. Evaluation of a technique for determining Re and PGEs in geological samples by ICP-MS coupled with a modified Carius tube digestion. Geochemical Journal 41, 407–414.

Qi, L., Wang, C.Y., Zhou, M.-F., 2008. Controls on the PGE distribution of Permian Emeishan alkaline and peralkaline volcanic rocks in Longzhoushan, Sichuan Province, SW China. Lithos 106, 222–236.

Qi, L., Zhou, M.-F., 2008a. Determination of platinum group elements in OPY-1: comparison of the results using different digestion techniques. Geostandards and Geoanalytical Research 32, 377–387.

Qi, L., Zhou, M.-F., 2008b. Platinum-group elemental and Sr–Nd–Os isotopic geochemistry of Permian Emeishan flood basalts in Guizhou Province, SW China. Chemical Geology 248, 83–103.

Shellnutt, J.G., Jahn, B.-M., 2010. Formation of the Late Permian Panzhihua plutonic–hypabyssal–volcanic igneous complex: implications for the genesis of Fe–Ti oxide deposits and A-type granites of SW China. Earth and Planetary Science Letters 289, 509–519.

Shellnutt, J.G., Pang, K.-N., 2012. Petrogenetic implications of mineral chemical data for the Permian Baima igneous complex, SW China. Mineralogy and Petrology 106, 75–88.

Shellnutt, J.G., Zhou, M.-F., 2007. Permian peralkaline, peraluminous and metaluminous A-type granites in the Panxi district, SW China: their relationship to the Emeishan mantle plume. Chemical Geology 243, 286–316.

Shellnutt, J.G., Jahn, B.-M., Zhou, M.-F., 2011. Crustally-derived granites in the Panzhihua region, SW China: implications for felsic magmatism in the Emeishan large igneous province. Lithos 123, 145–157.

Simkin, T., Smith, J.V., 1970. Minor element variation in olivine. Journal of Geology 78, 304–325.

Song, X.-Y., Zhou, M.-F., Cao, Z.-M., Robinson, P.T., 2004. Late Permian rifting of the South China Craton caused by the Emeishan mantle plume? Journal of the Geological Society of London 161, 773–781.

Song, X.-Y., Keays, R.R., Xiao, L., Qi, H.-W., Ihlenfeld, C., 2009. Platinum-group element geochemistry of the continental flood basalts in the central Emeishan large igneous province, SW China. Chemical Geology 262, 246–261.

Sun, S.-S., McDonough, W.F., 1989. Chemical and isotopic systematics in ocean basalt: implication for mantle composition and processes. In: Saunders, A.D.,

Norry, M.J. (Eds.), Magmatism in the Ocean Basins. Geological Society of London Special Publications, vol. 42. Blackwell Scientific Publication, Oxford, pp. 313–345.

Sun, Y.-L., Zhou, M.-F., Sun, M., 2001. Routine Os analysis by isotope dilution-inductively coupled plasma mass spectrometry: OsO_4 in water solution gives high sensitivity. Journal of Analytical Atomic Spectrometry 16, 345–349.

Tegner, C., Wilson, J.R., Brooks, C.K., 1993. Intraplutonic quench zones in the Kap Edvard Holm layered gabbro complex, East Greenland. Journal of Petrology 34, 681–710.

Wang, C.Y., Zhou, M.-F., Qi, L., 2007. Permian flood basalts and mafic intrusions in the Jinping (SW China)–Song Da (northern Vietnam) district: mantle sources, crustal contamination and sulfide segregation. Chemical Geology 243, 317–343.

Wang, C.Y., Zhou, M.-F., Qi, L., 2011. Chalcophile element geochemistry and petrogenesis of high-Ti and low-Ti magmas in the Permian Emeishan large igneous province, SW China. Contributions to Mineralogy and Petrology 161, 237–254.

Xiao, L., Xu, Y.G., Mei, H.J., Zheng, Y.F., He, B., Pirajno, F., 2004. Distinct mantle sources of low-Ti and high-Ti basalts from the western Emeishan large igneous province, SW China: implications for plume–lithosphere interaction. Earth and Planetary Science Letters 228, 525–546.

Xu, Y.G., Chung, S.L., Jahn, B.M., Wu, G.Y., 2001. Petrologic and geochemical constraints on the petrogenesis of Permian–Triassic Emeishan flood basalts in southwestern China. Lithos 58, 145–168.

Xu, Y.-G., He, B., Chung, S.-L., Menzies, M.A., Frey, F.A., 2004. Geologic, geochemical, and geophysical consequences of plume involvement in the Emeishan flood-basalt province. Geology 32, 917–920.

Zhang, Z., Mahoney, J.J., Mao, J., Wang, F., 2006. Geochemistry of picritic and associated basalt flows of the western Emeishan flood basalt province, China. Journal of Petrology 47, 1997–2019.

Zhang, Z., Mao, J., Saunders, A.D., Ai, Y., Li, Y., Zhao, L., 2009. Petrogenetic modeling of three mafic–ultramafic layered intrusions in the Emeishan large igneous province, SW China, based on isotopic and bulk chemical constraints. Lithos 113, 369–392.

Zhong, H., Zhu, W.-G., Chu, Z.-Y., He, D.-F., Song, X.-Y., 2007. Shrimp U–Pb zircon geochronology, geochemistry, and Nd–Sr isotopic study of contrasting granites in the Emeishan large igneous province, SW China. Chemical Geology 236, 112–133.

Zhong, H., Zhu, W.-G., Hu, R.-Z., Xie, L.-W., He, D.-F., Liu, F., Chu, Z.-Y., 2009. Zircon U–Pb age and Sr–Nd–Hf isotope geochemistry of the Panzhihua A-type syenitic intrusion in the Emeishan large igneous province, southwest China and implications for growth of juvenile crust. Lithos 110, 109–128.

Zhou, M.-F., Robinson, P.T., Lesher, C.M., Keays, R.R., Zhang, C.-J., Malpas, J., 2005. Geochemistry, petrogenesis and metallogenesis of the Panzhihua gabbroic layered intrusion and associated Fe–Ti–V oxide deposits, Sichuan Province, SW China. Journal of Petrology 46, 2253–2280.

Zhou, M.F., Arndt, N.T., Malpas, J., Wang, C.Y., Kennedy, A., 2008. Two magma series and associated ore deposit types in the Permian Emeishan large igneous province, SW China. Lithos 103, 352–368.

Zi, J.-W., Fan, W.-M., Wang, Y.-J., Cawood, P.A., Peng, T.-P., Sun, L.-H., Xu, Z.-Q., 2010. U–Pb geochronology and geochemistry of the Dashibao basalts in the Songpan–Ganzi Terrane, SW China, with implications for the age of Emeishan volcanism. American Journal of Science 310, 1054–1080.